6 Single-Molecule Biophysical Techniques to Study Actomyosin Force Transduction

Yasuharu Takagi, Nikolas Hundt, and Adam Fineberg

Abstract

Inside the cellular environment, molecular motors can work in concert to conduct a variety of important physiological functions and processes that are vital for the survival of a cell. However, in order to decipher the mechanism of how these molecular motors work, **single-molecule microscopy techniques** have been popular methods to understand the molecular basis of the emerging ensemble behavior of these motor proteins.

In this chapter, we discuss various single-molecule biophysical imaging techniques that have been used to expose the mechanics and kinetics of myosins. The chapter should be taken as a general overview and introductory guide to the many existing techniques; however, since other chapters will discuss some of these techniques more thoroughly, the readership should refer to those chapters for further details and discussions. In particular, we will focus on scattering-based single-molecule microscopy methods, some of which have become more popular in the recent years and around which the work in our laboratories has been centered.

Keywords

Single molecule microscopy techniques · *In vitro* actin gliding assay · Single molecule fluorescence microscopy (SMFM) · Optical trap or tweezer (OT) · Dark-field microscopy · Interferometric scattering (iSCAT)

Y. Takagi (✉)
Laboratory of Molecular Physiology, Center for Cell and Developmental Biology, National Heart, Lung, and Blood Institute (NHLBI), National Institutes of Health (NIH), Bethesda, MD, USA
e-mail: takagiy@mail.nih.gov

N. Hundt
Department of Cellular Physiology, Ludwig-Maximilians-Universität München, Munich, Germany
e-mail: nikolas.hundt@med.uni-muenchen.de

A. Fineberg
Physical and Theoretical Chemistry Laboratory (PTCL), Department of Chemistry, University of Oxford, Oxford, UK
e-mail: adam.fineberg@chem.ox.ac.uk

6.1 Why Use Single-Molecule Assays?

Single-molecule techniques have been employed in the actomyosin/cytoskeletal field for the last 30+ years. These methods have been very popular in this field, because it was generally difficult to decrypt the molecular details of how individual proteins function from ensemble or bulk measurements. In ensemble experiments, the measured variable is usually an average over the

L. M. Coluccio (ed.), *Myosins*, Advances in Experimental Medicine and Biology 1239,
https://doi.org/10.1007/978-3-030-38062-5_6

entire population of molecules. More critically, the observables are often large scale solution properties, such as light absorption, scattering, fluorescence and conductivity, which can change in response to a molecular behavior, but they do not visualize the molecular behavior itself. This limits the interpretation of the underlying mechanism. For instance, it would require some basic understanding of the system if an increase in light scattering of a solution of actin were to be interpreted as a polymerization into filaments. For myosins, it would require a large array of different experiments to conclude that a motor walks processively along actin filaments. Using single-molecule techniques, however, these mechanisms become immediately apparent. One can then even start to probe molecular behavior on a molecule-by-molecule basis, which allows the characterization of sub-populations and ultimately leads to the understanding of the resultant bulk behavior from a "bottom-up" perspective.

In recent decades or so, single-molecule techniques have become so advanced that dynamic behavior of proteins can be measured with angstrom level spatial resolution and micro-second temporal resolution. This information can be used to draw a detailed picture of how conformational changes are linked to enzymatic activity and in the case of molecular motors to directed force production. In combination with structural studies, single-molecule techniques can decipher molecular dynamics at the atomic level and make it possible to even understand design principles that can be used to build artificial molecular motors (Chen et al. 2012; Furuta et al. 2017; Furuta and Furuta 2018).

6.2 The Original Assays – Bead Motility and *in vitro* Actin Gliding Assays

To understand the advances in single-molecule microscopy techniques utilized in the actomyosin field, we have to first step back and discuss an ensemble microscopy assay that has become the "granddaddy of them all": the myosin motility assay.

Initial experiments to understand the mechanical activity of myosins used an assay geometry whereby native actin bundles (*i.e.,* polar actin cables of the alga *Nitella axillaris)* (Sheetz and Spudich 1983; Vale et al. 1984) or stereocilia from bullfrog sacculi and semicircular canals (Shepherd et al. 1990)) were adhered to a coverslip glass as tracks for myosins attached to large polystyrene beads, the motion of which could be followed under a microscope. An illustration of this assay is shown in Fig. 6.1. In the presence of ATP, these beads moved along the actin filament bundles in a processive unidirectional manner (Sheetz and Spudich 1983; Sheetz et al. 1986; Hynes et al. 1987). This bead motility assay was the first practical and quantitative assay to determine the motion of ensembles of myosins and was also used as a prototype system for future single-molecule assays in the late 1980's/early 1990's.

The second type of assay, the *in vitro* actin-gliding assay, was first shown to work by the Spudich group (Kron and Spudich 1986). Here, myosin motion was measured using a purified protein system (*in vitro*) in a chamber with essentially myosin, actin filaments and ATP. This was similar to the bead motility assay but used purified individual actin filaments instead of bundled actin filaments.

In this assay, flow cells were constructed with a microscope coverslip coated on one surface with either rabbit skeletal muscle myosin or *Dictyostelium discoideum* myosin. A mixture of fluorescent phalloidin-labeled actin filaments together with ATP was then infused into the flow cell. The motion of the fluorescently-labeled actin filaments, propelled by the surface-attached myosins, was observed using a microscope equipped with a wide-field fluorescence imaging modality (Fig. 6.2). Videos of the actin filaments' motion were saved on video-tapes for further analysis such as to determine actin filament lengths, velocities and distances traveled. More details on the assay can be found in a methodology paper by Kron et al. (1991).

In vitro actin gliding formed the basis of the single-molecule mechanical and kinetic assays, whereby a simplified system with only actin fila-

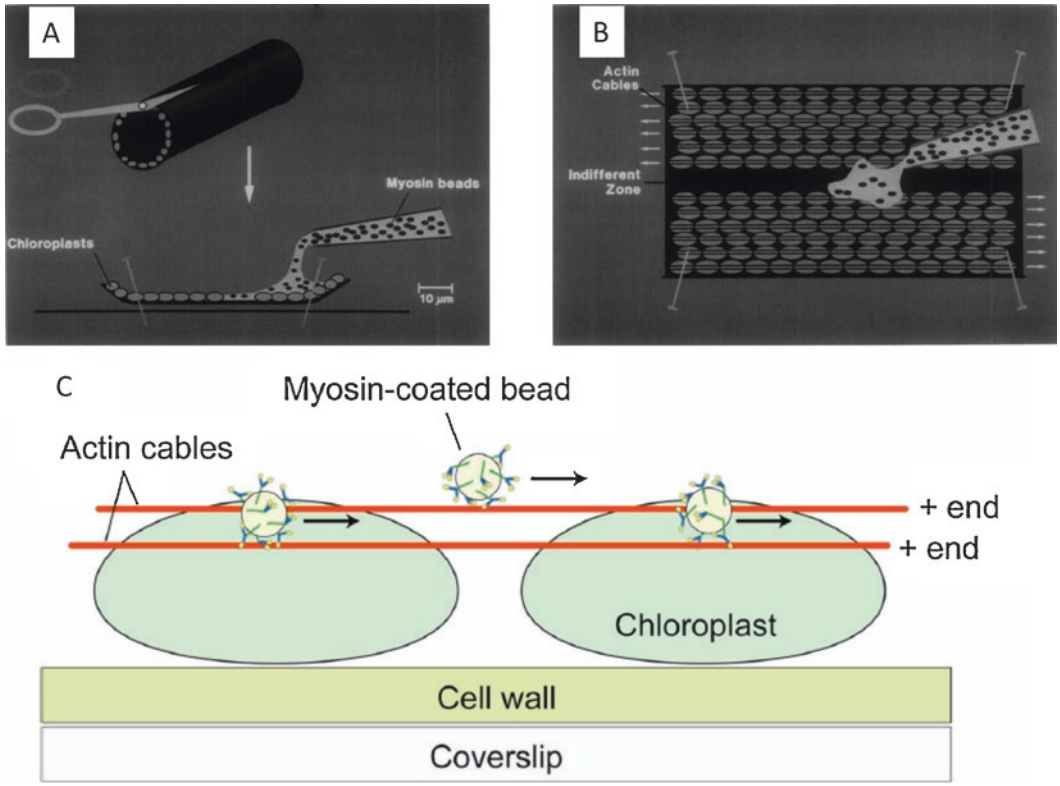

Fig. 6.1 Bead motility assay. (**a**) Diagram showing cutting of the cylindrical *Nitella* cell, pinning of the cut cell, and deposition of the myosin-attached beads. (**b**) Diagram showing the open cell from the top. Arrows indicate direction of movement of vesicular elements *in vivo*. Myosin-2-coated beads move in the same direction *in vitro*. (**c**) Diagram showing the motion of the myosin-2-coated beads on the actin cables. (Diagrams reproduced from Sheetz et al. 1986 and Kodera and Ando 2014. Copyright 1986 Elsevier BV)

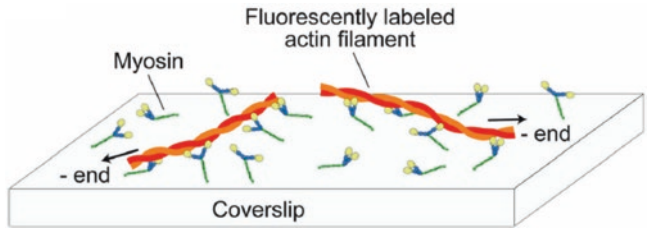

Fig. 6.2 *in vitro* actin gliding assay. Diagram illustrating the motion of the fluorescently-labeled actin filaments on a bed of myosins attached to the surface. (Diagram reproduced from Kodera and Ando 2014)

ments and myosin is reconstituted inside a microscope flow cell. Over time, advances in the theoretical understanding of the underlying processes have produced variations of this assay in which other actin-binding proteins apply loads to the propelled actin filaments by retarding their movement (Warshaw et al. 1990; Bing et al. 2000; Greenberg and Moore 2010; Aksel et al. 2015). This variation of the assay has been used to investigate the response of myosin ensembles to external forces.

In recent years, in order to quantitatively analyze *in vitro* actin gliding data, new programs such as FIESTA and FASTA have been devel-

oped (Ruhnow et al. 2011; Aksel et al. 2015) making analysis easier and more efficient. However, other "analog" motion analysis type modules have been utilized to quantify data in a similar fashion since the 1990's (Homsher et al. 1992; Sellers et al. 1993).

For measuring the mechanics of higher-order myosin macromolecular complexes such as myosin-2 assembled into bipolar filamentous structures, experiments have been performed by attaching native molluscan myosin-2 "thick filaments" onto a glass surface and measuring the actin filaments moving above them (Sellers and Kachar 1990). These experiments used a combination of differential interference contrast (DIC) and wide-field fluorescence microscopy to visualize the myosin thick filaments and actin, respectively. As expected from the bipolar structure of the myosin filament, the actin filaments were seen to move towards the center of the thick filaments. The study showed that the actin filaments moved on the myosin filament structure towards the center of the bare zone at a rate of ~9 μm s^{-1}. Contrary to this expected direction of motion, the authors also showed that the actin filaments can move from the center bare zone towards the outside of the bipolar myosin filament but at a slower velocity, ~1 μm s^{-1}. This result suggested that any given orientation of the actin filament could interact with any portion of the myosin filament and contribute to the force generation process. This assay topology has been used in a recent study of cardiac myosin-2 in the presence of a variety of wild-type and mutant cardiac myosin binding protein-C (Previs et al. 2012) to show how cardiac myosin-binding protein-C modulates cardiac contractility.

Myosin filament-based assays can also be used in an "inverted" geometry where the actin filaments are bound to the surface and the movement of the myosin filaments is observed. In recent years, such experiments have been performed with smooth, skeletal and cardiac myosin-2 (Brizendine et al. 2015; Brizendine et al. 2017), as well as non-muscle myosin-2A and myosin-2B filaments (Nagy et al. 2013; Melli et al. 2018) to decipher the molecular mechanism of force generation and motion of these filament complexes as a more physiological motile unit.

All of these "motor ensemble" *in vitro* motility assays developed in the 1980's-90's laid the foundation for the single-molecule microscopy assays performed in the following decades.

6.3 Early Days of Single-Molecule Fluorescence Assays

When light propagates through a medium such as a glass coverslip and encounters a medium of lower refractive index such as water or buffer, it is either refracted or reflected depending upon the angle of incidence and the difference in refractive indices of the two media. At the critical angle, *i.e.* ~62° for a glass/water interface, where light is totally internally reflected, an evanescent wave extends into the aqueous medium whose intensity falls exponentially with penetration depth (~100 nm), thus illuminating only a shallow volume above the interface.

This fluorescence technique, called **T**otal **I**nternal **R**eflection **F**luorescence (TIRF) microscopy, allows only the fluorophores that are very close to the interface to be excited without exciting the "background" fluorophores that are not reached by the evanescent wave. This technique achieves an increased signal-to-noise ratio of the intensity of fluorophores that are very close to the coverslip. Different optical paths, or methods, to accomplish TIRF microscopy have been described previously in Axelrod 2001 and Axelrod 2008, which can be referred to for more details (Fig. 6.3).

Single-molecule fluorescence measurements of myosins began with an article published in 1995 by the Yanagida group who used TIRF microscopy to visualize single molecules of skeletal muscle heavy meromyosin (HMM) labeled with a Cy3 dye and bound to a coverslip surface (Funatsu et al. 1995). The authors demonstrated that the fluorescence of the observed "myosin" spots disappeared in either one or two quantal steps of photobleaching, providing evidence that either one or two fluorophores were covalently

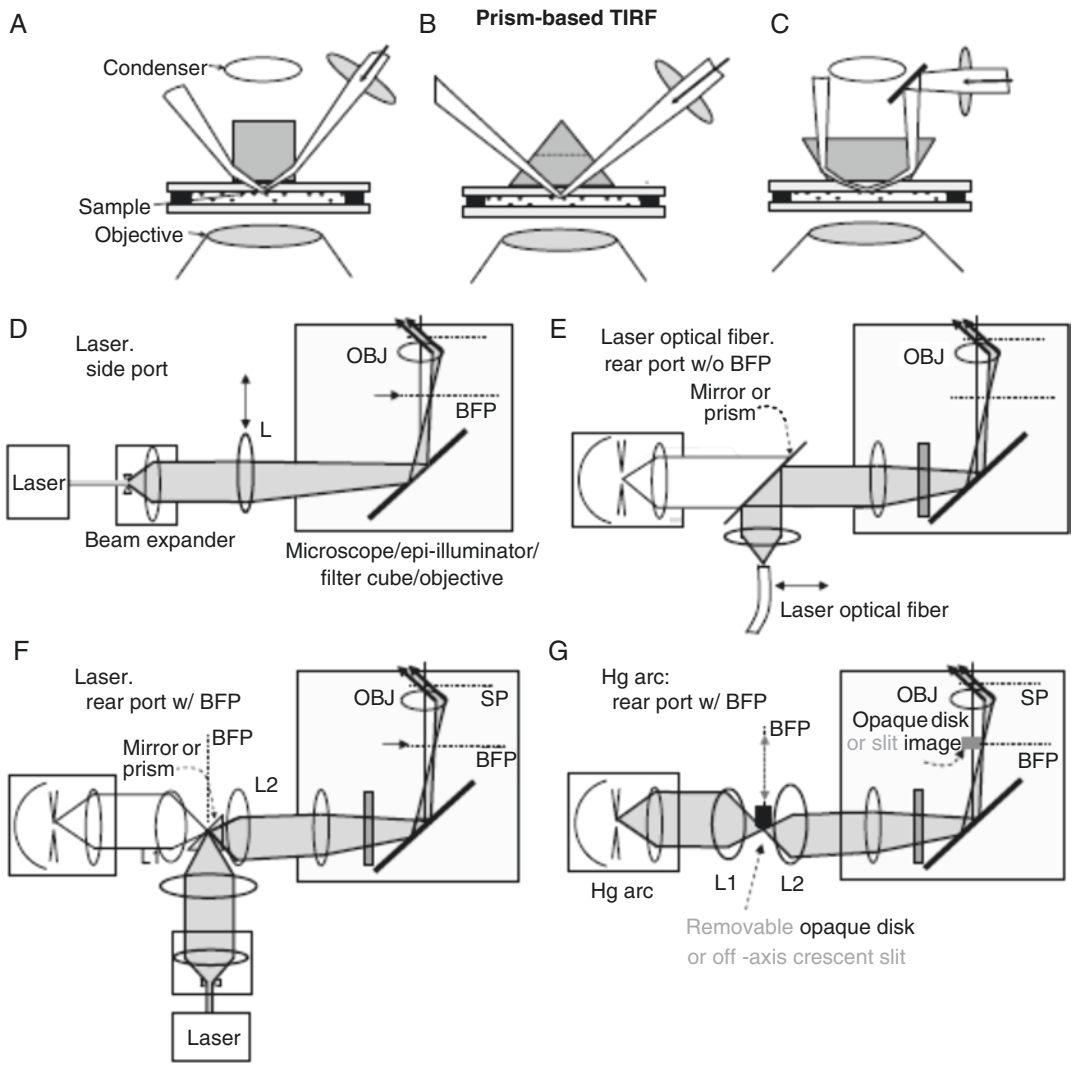

Fig. 6.3 TIRF microscopy examples. (**a**–**c**) Schematic illustrations of different types of prism-based TIRF microscopy. Sample chambers can be made as a "sandwich" with a lower glass coverslip, a spacer such as Teflon or double-sided sticky tape and a coverslip with sample which is mounted upside-down so that the sample faces downwards. The outer surface of the sample coverslip is put into contact with a prism through a film of immersion oil. (**d**–**g**) Schematic illustrations of different objective-type TIRF in an inverted microscope. (**d**) Laser illumination from the side port using a dichroic mirror cube facing towards the side port. The beam is focused onto the BFP at a radial position sufficient to lead to supercritical angle propagation at the coverslip. Transverse motion of L can be used to alter between epi-fluorescence and TIRF modes. (**e**) Laser illumination using an optical fiber, through the rear port. (**f**) Laser illumination using an equivalent BFP in some microscope systems to focus the beam. Another equivalent back focal plane sometimes marked as the aperture lane exists in some systems. (**g**) An arc lamp can be used for total internal reflection illumination, too. For more details on these schemes, please refer to Axelrod 2001 and Axelrod 2008. OBJ = objective lens, SP = sample plane, BFP = back focal plane, L = focusing lenses. (Diagram reproduced from Axelrod 2008. Copyright 2008 Elsevier BV)

bound to the molecule. Furthermore, they explored the binding and dissociation of Cy5-labeled ATP using TIRF microcopy and found that lifetimes of merging Cy3/Cy5 spots were consistent with the known kinetics of binding, hydrolysis and release of ATP by the myosin.

6.4 Single-Molecule Fluorescence Assays Using Enhanced Localization Techniques

The movement of processive molecular motors was commonly studied using the inverted geometry of the *in vitro* actin gliding assay, with the actin filaments bound to the surface of the image plane, such that the motion of these molecular motors could be observed. Rather than linking a large bead to myosins as in the early studies from the 80's described above, scientists created other methods to "tag" a protein with fluorescent probes so that the motion of the protein could be inferred from the motion of the attached marker. Genetically encoded fluorophores (such as green fluorescent protein (GFP) or enhanced GFP (eGFP)) (Snyder et al. 2004; Yildiz et al. 2004b), an accessory protein (i.e., calmodulin) attached to an organic dye (Forkey et al. 2003; Yildiz et al. 2004b; Sakamoto et al. 2005) or quantum dots (Qdots) (Warshaw et al. 2005; Ali et al. 2007) were a few examples of how researchers attached fluorophores to the myosin.

6.4.1 FIONA

At first, TIRF-based inverted single-molecule motility assays were used to measure only velocities and run lengths of individual myosins over actin filaments fixed to the surface (Sakamoto et al. 2000, 2003). However, the detailed translocation, or stepping, mechanism at the nanometer resolution was still unresolved using fluorescence techniques.

In microscopy, Abbe's law dictates that in order for two objects to be resolved they must be separated by a distance $\Delta x \geq \frac{\lambda}{2 \cdot NA}$, where λ is the wavelength of light and NA is the numerical aperture of the objective lens. This separation distance is thus typically around 200–350 nm for visible light ($\lambda \sim 400$–750 nm), which also defines the width of the imaged spots of the fluorophores or the so-called point spread function (PSF). In order to overcome this limit, a method was developed that used the shape of the PSF to localize fluorescent probes at higher precision than was dictated by Abbe's diffraction limit (Yildiz et al. 2003) and was applied to studying the detailed mechanics of myosin-5a translocation.

This method, named FIONA for ***F***luorescence ***I***maging at ***O***ne ***N***anometer ***A***ccuracy, allowed the specificity and sensitivity of single-molecule fluorescence with nanometer localization precision of the position of the fluorophore. The two-dimensional PSF of a fluorophore was observed such that sufficient photons (~5000–10,000) were collected per diffraction limited PSF of a single fluorophore. A Gaussian fit to the PSF was used to localize the average position of the fluorophore to approximately 1.5 nanometer accuracy.

The mathematical expression for this emission intensity distribution was described as a two-dimensional Gaussian in the form:

$$I(x,y) = I_{Background} + A \exp\left\{-\frac{1}{2}\left[\frac{x-x_0}{S_x}\right]^2 - \left[\frac{y-y_0}{S_y}\right]^2\right\}, \tag{6.1}$$

where $I_{Background}$ is the background intensity (or noise floor), x_0 and y_0 describe the coordinates of the center position of the fluorophore, and S_x and S_y are the standard deviations of the distribution in both directions.

The width, or the standard error of the mean, $\sigma^{\mu}_{x,y}$, of this distribution can be described as:

$$\sigma^{\mu}_{x,y} = \sqrt{\frac{S^2_{x,y}}{N_{Photons}} + \frac{a^2}{12 \cdot N_{Photons}} + \frac{8 \cdot \pi \cdot S^4_{x,y} \cdot b^2}{a^2 \cdot N_{Photons}}}, \tag{6.2}$$

where, $N_{Photons}$ is the number of collected photons, a is the pixel size of the image detector and b is the standard deviation of the background fluctuations (Thompson et al. 2002; Yildiz et al. 2003).

The first term in Eq. 6.2, $\frac{S^2_{x,y}}{N_{Photons}}$, is the photon noise; the second term, $\frac{a^2}{12 \cdot N_{Photons}}$, is the effect

of the pixel size of the detector; and the third term, $\frac{8 \cdot \pi \cdot S_{x,y}^4 \cdot b^2}{a^2 \cdot N_{Photons}}$, is the effect caused by background fluctuations. Thus, for a photon noise limited case – *i.e.,* when the noise in each pixel is dominated by photons originating from the particle being localized – the equation above can be reduced to show that the expression for the best estimate of the position of the fluorophore is:

$$\left(\Delta x\right)^2 = \frac{S_{x,y}^2}{N_{Photons}}, \tag{6.3}$$

where Δx is the error in localization, $S_{x,y}$ is the standard deviation of the point-spread function and $N_{Photons}$ is the number of photons collected. Thus, increasing the number of collected photons leads to lower localization uncertainty. In this case ~1.5 nm localization precision was achieved by collecting ~10,000 photons per diffraction limited spot, or fluorophore (Fig. 6.4).

This ability to achieve a high localization precision, together with the observation that certain fluorophores undergo blinking, was the starting point for imaging techniques later developed for use in cell biological studies such as photoactivated localization microscopy (PALM) (Betzig et al. 2006) and stochastic optical reconstruction microscopy (STORM) (Rust et al. 2006; Huang et al. 2008).

The results with myosin-5a using FIONA led to the development of a model in which the motor steps in a hand-over-hand motion, taking alternating step sizes between 37 + 2x and 37 − 2x nm, where x is the distance along the direction of motion between the dye and the midpoint between the two heads (Yildiz et al. 2003) (Fig. 6.5). The same "super-resolution" localization method has been applied to other cytoskeletal motor systems such as kinesin (Yildiz et al. 2004a) and dynein (Reck-Peterson et al. 2006).

6.4.2 Two Fluorophore Super-Resolution Fluorescence Imaging

With the development of FIONA, other single-molecule localization methods to determine distances have emerged such as ***S***ingle-molecule ***H***igh-***R***esolution ***Im***aging with ***P***hotobleaching (SHRImP) (Gordon et al. 2004) and ***NA***nometer-***L***ocalized ***M***ultiple ***S***ingle-molecule fluorescence microscopy (NALMS) (Qu et al. 2004). These methods were conceived to measure distances between two identical fluorophores in the range of 10–200 nm using photobleaching. Similarly, ***S***ingle-molecule ***H***igh ***RE***solution ***C***olocalization (SHREC) was developed to measure intramolecular distances using two different fluorophores (Churchman et al. 2005). Both SHRImP and SHREC have been used extensively to observe the stepping mechanics of myosin-5a and myosin-6 (Churchman et al. 2005; Warshaw et al. 2005; Balci et al. 2005). Figure 6.6 shows an example of a dual Qdot-labeled myosin-5a with head spacing of ~36 nm measured by the distances between the two Qdots, and step size of 72 nm calculated from tracking one Qdot over time.

6.4.3 *pol*TIRF

Nanometer measurements of intramolecular domain distances and stepping patterns have been extremely useful for understanding how motor proteins work. Moreover, detecting the rotational dynamics of myosins has been another direction for single-molecule fluorescence microscopy development that has advanced our understanding of the mechanisms behind force and motion generation in myosins. On this avenue, fluorescence polarization techniques have been used extensively to probe the angular changes of the lever arm domain of myosins during their enzymatic cycle. *pol*TIRF or ***pol***ar-

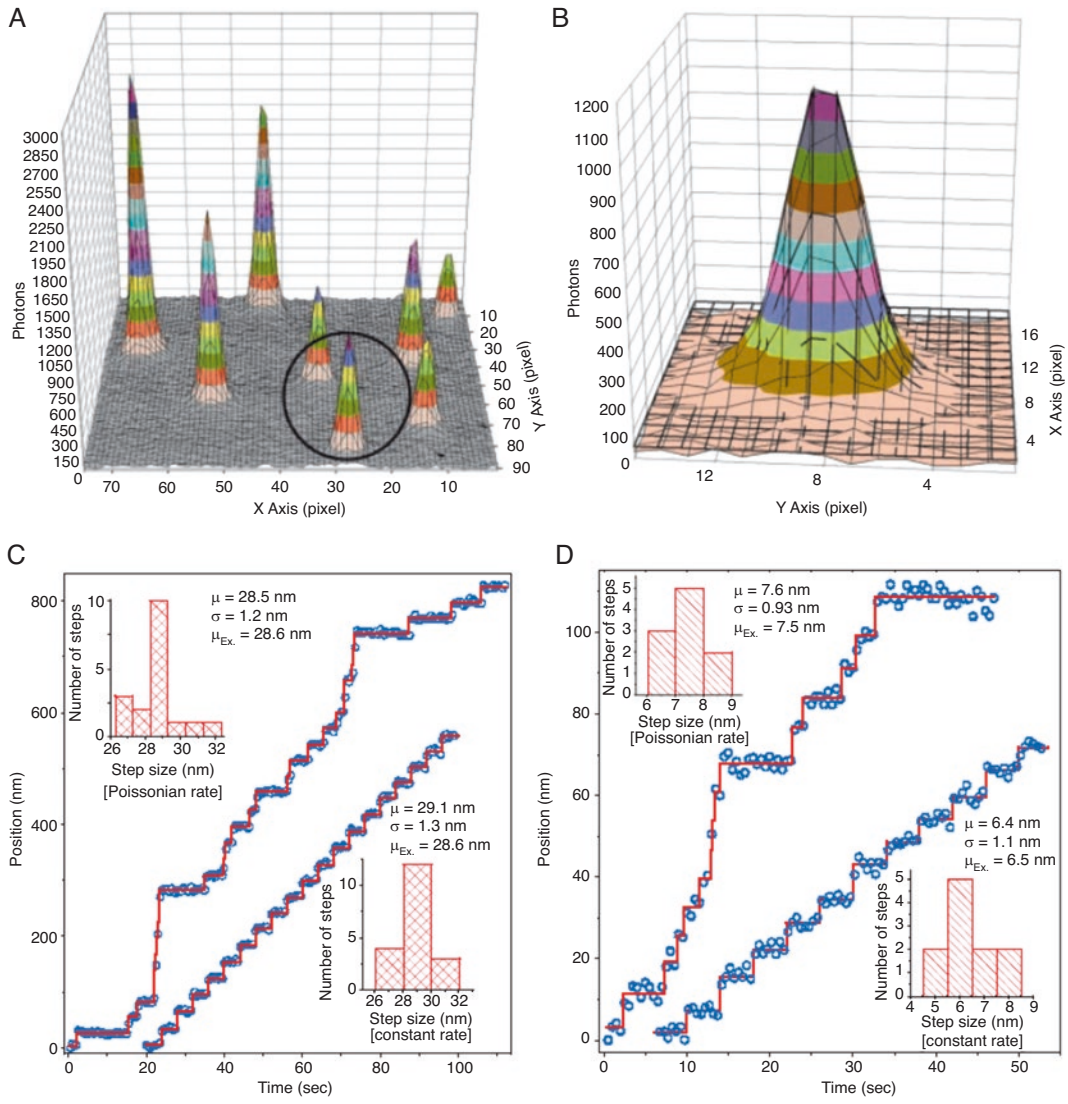

Fig. 6.4 FIONA example – Cy3. (**a**) Point-spread functions (PSF) of individual Cy3 molecules attached to a coverslip with 0.5 s integration time. (**b**) Gaussian fit to the PSF, with center position determined at 1.3 nm precision. Width of PSF is 287 nm. (**c** and **d**) Coverslip with Cy3 dye molecules were moved using the piezo-stage, using a constant or a Poisson distributed rate, while the PSF of the dyes were tracked. Precision is approximately 1 nm. (Diagram reproduced from Yildiz et al. 2003. Copyright 2003 Science/AAAS)

ization ***T***otal ***I***nternal ***R***eflection ***F***luorescence microscopy (Fig. 6.7) is an imaging modality that takes advantage of the polarized characteristic of the emission dipole of the fluorophore with respect to the excitation laser or incident light source. *pol*TIRF microscopy has been performed using a prism-type TIRF microscope arrangement, allowing complex combinations of multiple input laser paths and polarizations for fluorophore excitation in the field-of-view of the microscope. Emission of the fluorophores in different polarizations are monitored using avalanche photodiodes (APDs). Using this method, it was possible to measure the rotational motion of a fluorophore (bifunctional rhodamine) attached to the calmodulin on the lever arms of myosin-5 (Forkey et al. 2003) and myosin-6 (Sun et al. 2007), as well as myosin-10 (Sun et al.

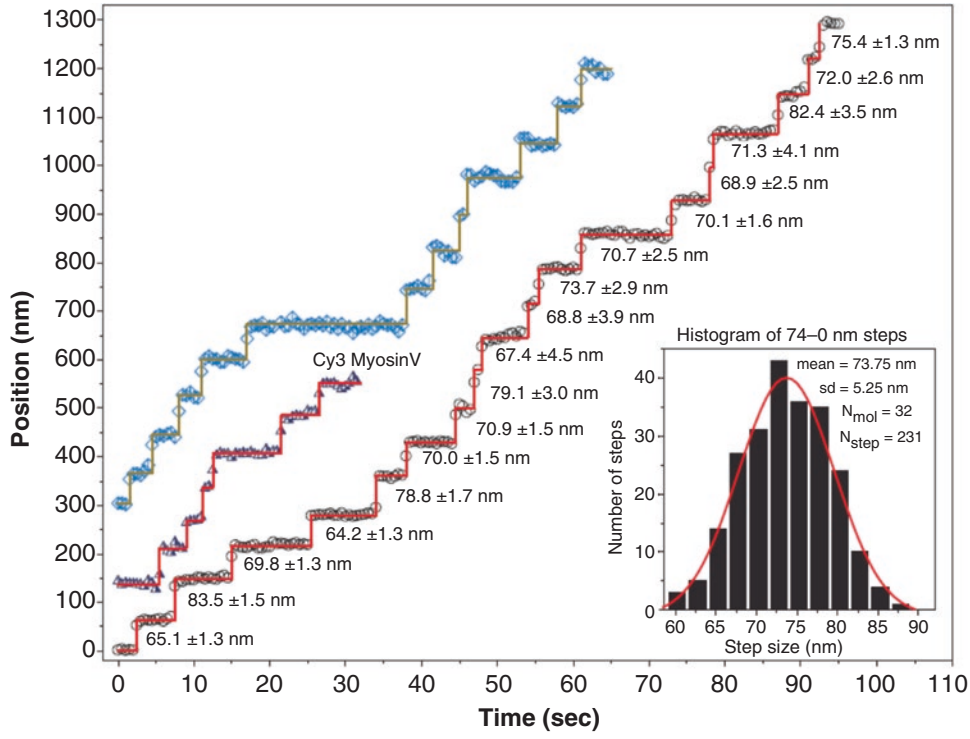

Fig. 6.5 FIONA example – Myosin-5a. Stepping trajectory of three different myosin-5a molecules, displaying ~74 nm steps since only one of the lever arms was labeled with a bifunctional rhodamine or Cy3 dye. Histogram of all steps (inset) confirms an average step size of ~74-nm. (Diagram reproduced from Yildiz et al. 2003. Copyright 2003 Science/AAAS)

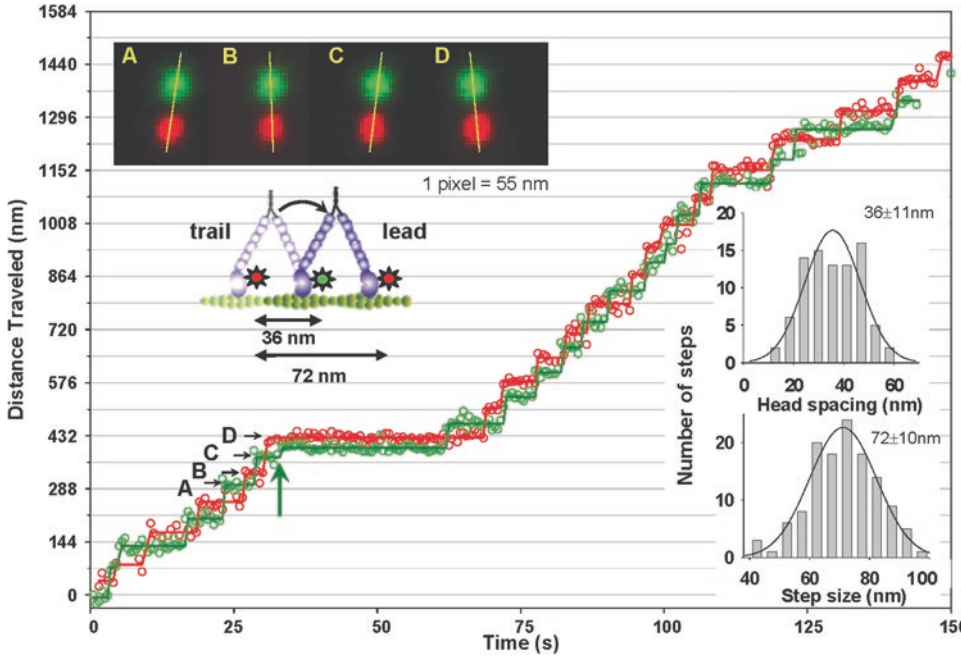

Fig. 6.6 SHREC – Myosin-5a with Qdots. Myosin-5a with a biotinylation site on the motor domain was labeled with Qdot 565 (Green) and Qdot 655 (Red). Upper left image shows the averaged Qdot images for the steps labeled **A** to **D** with the two-color images offset vertically for clarity. The yellow lines emphasize the alternating relative head positions. Inset histograms show inter-head spacing (~36 nm average) and step-size (~72 nm average). (Diagram reproduced from Warshaw et al. 2005. Copyright 2005 Elsevier BV)

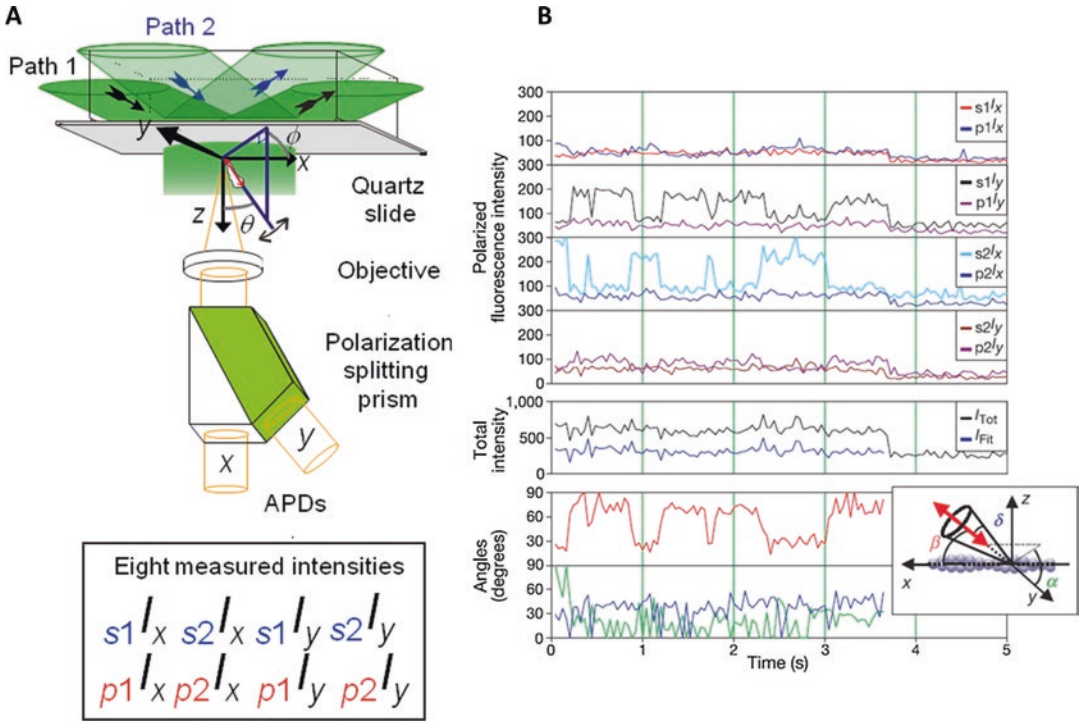

Fig. 6.7 *pol*TIRF-scheme and myosin-5a. (**a**) Scheme for single-molecule polTIRF setup. Dual path illumination of an input laser is used to create an evanescent wave at the sample surface using a prism –type TIRF microscope. Emission of a fluorophore is collected using an objective lens and passed through a polarization splitting prism. A pair of avalanche photodiodes is used to collect the x- and y-polarized fluorescent emissions. This configuration of the polTIRF allows collection of 8 different combinations of polarized excitation/emission intensities. Further analysis of these measurements allows interpretation of single-molecule rotational motion of the studied fluorophores. (Image from Rosenberg et al. 2005. Copyright 2005 American Chemical Society). (**b**) polTIRF data of a single molecule of myosin-5a labeled with a bifunctional rhodamine-labeled calmodulin moving along an actin filament. Polarized fluorescence intensities ($_{s}I_{\_}$ and $_{p}I_{\_}$; units = photocounts per 10 ms gate) and total intensity ($I_{\_}$; units = photocounts per 40 ms cycle) are shown (upper four graphs). The first subscripts, $_{s\_}$ and $_{p\_}$, describe the linear excitation polarizations along the x- and y- axes and the excitation polarizations approximately along the z-axis, respectively. The second subscripts represent the detection polarization in the x- and y-axes of the experimental coordinate system. Measurements are used to define the motion of the labeled calmodulin bound to myosin-5a during translocation *via* the β, α and δ angles (represented as red, green and blue; lower two graphs). The β angle shows two distinct angles of the probe, representing the tilting of the lever arm between two structural states. The inset (bottom right) defines these angles relative to the actin filament and the polTIRF apparatus coordinate systems as shown. (Images from Forkey et al. 2003. Copyright 2003 Nature Publishing Group)

2010). More details can be found in the following articles and reviews about this method (Forkey et al. 2000, 2003; Beausang et al. 2012, 2013).

6.4.4 DOPI

DOPI, or ***D***efocused ***O***rientation and ***P***osition ***I***maging, another twist on the single-molecule localization method (Toprak et al. 2006), was developed to quantify the rotational motion, or orientation, of a fluorescent probe while simultaneously measuring its position. The rotational orientation of the fluorophore was determined by imaging a defocused PSF (Fig. 6.8). By tracking the translational and rotational motion of a single bifunctional rhodamine probe attached to one of the calmodulins of the light-chain binding domain (LCBD) of myosin-5, it was found that the rhodamine probe dwelled in two distinct ori-

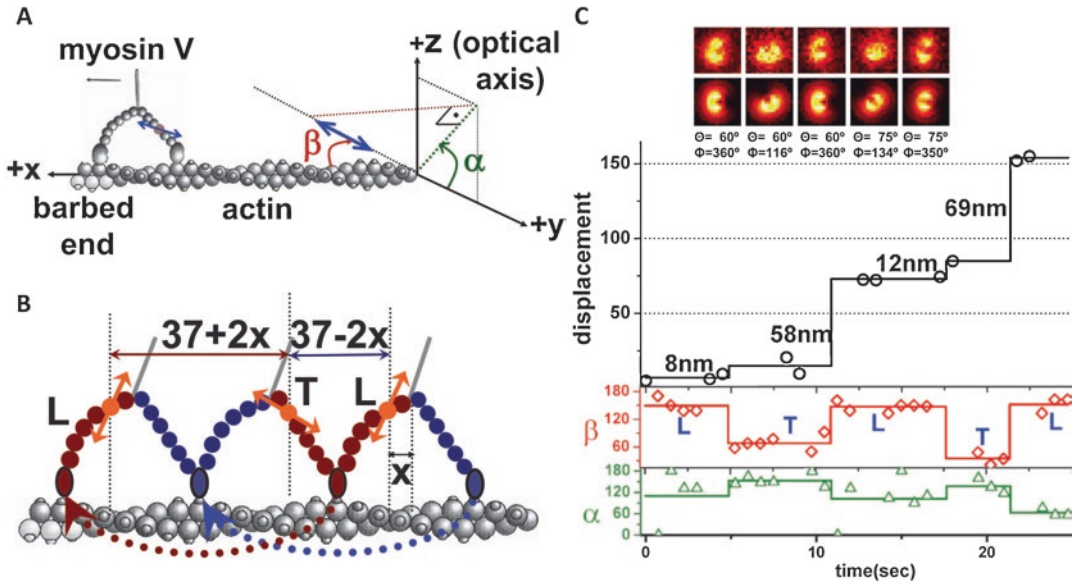

Fig. 6.8 DOPI – Myosin-5a. (**a**) Actin-based coordinate system used to analyze the relative motion of the dye attached to myosin-5a. (**b**) Cartoon of myosin-5 undergoing two steps, showing the tilting emission dipoles of the dye attached to one of its IQ motifs (orange arrow). (**c**) DOPI (3D orientation) and FIONA (displacement) data for single molecules of myosin-5a. Figures show data from two different myosin-5a molecules stepping on average 64–10 nm (first step – second step). The differences in stepping distances are due to the multiple positions where the labeled calmodulins can be bound on the lever arm. Upper panels are the images of the labeled myosin-5a. Second panel from top are the FIONA stepping data. Third and fourth from top show the β and α angles determined from fitting the images in the top panel. (Images from Toprak et al. 2006. Copyright 2006 National Academy of Sciences, USA)

entations. These dwells coincided with two distinct step sizes which could be explained by the asymmetric positioning of the calmodulin bound to one of the myosin-5 heavy chain's LCBD on the lever arm, which was then alternating between the leading and trailing position.

6.5 Scattering-Based Microscopy

The field has gained considerable insight into the molecular details of myosin stepping mechanisms from single-molecule fluorescence studies. However, some of the conformational transitions in myosins, such as the diffusive period of a detached motor domain during a processive walk, happen at the timescale of a few ms down to μs. Although fluorescence-based imaging has enabled the localization of single motors down to a precision of a nanometer (see FIONA), the fundamental physics of the fluorescent process eventually limit the achievable precision and time resolution as it becomes more and more difficult to capture a sufficient number of photons (Eq. 6.3). The maximum speed of the excitation-emission cycle of a fluorophore is dictated by its photophysics. Many fluorophores can also return to their ground-state without emitting a photon at all. Oxidative stress and photobleaching further hamper the quest for an ever-higher imaging speed that requires more and more incident light.

The process of light scattering is not affected by these fundamental limits of fluorescence, as the number of scattered photons simply scales with the number of incident photons. Theoretically, the detection in scattering is therefore only limited by the light intensity that can be directed onto the sample. In practice, however, scattering-based detection has a major disadvantage over fluores-

cence, which has probably been the main reason for its lower popularity. While the signal in fluorescence measurements is specifically generated by the fluorophore and all background signal is suppressed through optical filters, scattered light is produced by all species in a sample, which therefore all contribute to the detected signal. This makes it crucial for scattering-based single-molecule studies to have a strategy for removal of any unwanted background.

As mentioned in previous chapters, most single-molecule myosin experiments operate at a glass-water interface (Deniz et al. 2007). If light is directed onto such a sample, a glass-water interface will reflect 0.4% of the incident illumination (Hecht 1998). The light that is not reflected will then be scattered by any object with a different refractive index to the surrounding medium, in this case, the aqueous solution. The intensity, I_{det}, detected by the camera depends on the amplitudes of the reflected electric field including other background light, $\mathbf{E}_r$, and the scattered electric field, $\mathbf{E}_s$, as well as their relative phases φ:

$$I_{\text{det}} = \left|\mathbf{E}_r + \mathbf{E}_s\right|^2 = \left|\mathbf{E}_r\right|^2 + \left|\mathbf{E}_s\right|^2 + 2\left|\mathbf{E}_r\right|\left|\mathbf{E}_s\right|\cos\varphi \tag{6.4}$$

Equation (6.4) shows the three contributions to the detected intensity: the reference and background signal, $|\mathbf{E}_r|^2$, the scattering signal, $|\mathbf{E}_s|^2$, and an interference term, $2|\mathbf{E}_r||\mathbf{E}_s|\cos\varphi$.

To date, researchers have used two different scattering-based microscopic techniques to study myosin dynamics, dark-field (DF) microscopy and interferometric scattering microscopy (iSCAT).

Dark-field microscopes operate by reducing the background light, $|\mathbf{E}_r|^2$, so as to make the pure scattering signal, $|\mathbf{E}_s|^2$, the dominant term in Eq. (6.4). This produces a dark image with bright scattering objects.

Interferometric scattering microscopy, on the other hand, does not exclude all background light and uses the large signal from the glass-water interface as a reference field. For sufficiently small scatters, $|\mathbf{E}_s|^2$ becomes negligible and therefore the detected signal is the interference term, $2|\mathbf{E}_r||\mathbf{E}_s|\cos\varphi$, on top of a bright background, $|\mathbf{E}_r|^2$.

6.5.1 Dark-Field Microscopy

As early as 1903, scattering was used as a contrast mechanism to visualize colloidal gold particles (Siedentopf and Zsigmondy 1903). The pioneering researchers used a so-called "ultramicroscope" to collect light from a sample at a 90° angle from the illuminating beam path. This earliest example highlights the general principle of dark-field microscopy in which all background light is rejected while the pure scattering contribution is detected. In this regard, dark-field microscopy is technically similar to fluorescence microscopy, only the strategy of attenuating the background illumination has to be adjusted, since the scattered light is not spectrally shifted as it usually is in fluorescence.

In modern commercial dark-field microscopes, the illuminating light is usually focused onto the sample through a condenser (Gage 1920) as shown in Fig. 6.9a by which the light can be seamlessly shifted into and away from the detecting optic. This way the user can easily switch between bright- and dark-field imaging (Fig. 6.9a).

Other more recent strategies use laser beams that are coupled into the back focal plane of an objective and illuminate the sample in total internal reflection (Nishikawa et al. 2010; Ueno et al. 2010; Mickolajczyk and Hancock 2018). The illuminating beam in these setups is directed into the objective using perforated mirrors (Nishikawa et al. 2010; Ueno et al. 2010) or micro-mirrors (Mickolajczyk and Hancock 2018) that leave space for the scattering image to be picked up into the detecting beam path while excluding the illuminating light (Fig. 6.9b and c).

Revisiting Eq. (6.4), dark-field microscopy rejects all background light from the sample and collects the pure scattering signal, reducing the expression to:

$$I_{\text{det}} = \left|\mathbf{E}_s\right|^2 = \left|\mathbf{E}_i\right|^2 \cdot \left|s\right|^2, \tag{6.5}$$

where $\mathbf{E}_i$ is the electric field of incident light upon the sample and s is the complex scattering amplitude. As the scattering intensity is directly proportional to the intensity of the incident light,

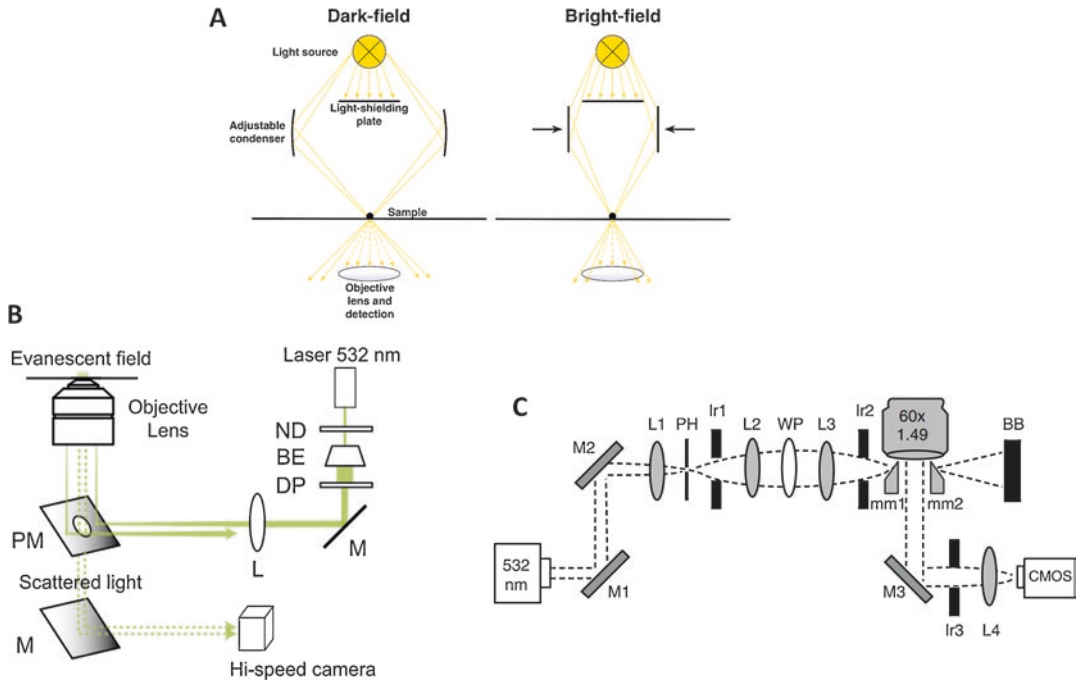

Fig. 6.9 Dark-field microscopy setups. (**a**) Schematic of commercial darkfield microscopes that are able to gradually switch between dark-field and bright-field by shifting the adjustable condenser. (**b**) TIRDF by Ueno et al. 2010 with perforated mirror (PM). ND = neutral-density filter, BE = beam expander, DP = diaphragm, M = mirror, L = lens. (**c**) Micro-mirror (mm) TIRDF by Mickolajczyk and Hancock 2018. M = mirror, L = lens, PH = pinhole, Ir = iris, WP = half-wave-plate, BB = beam blocker. (Images used with permission. Copyright 2010 Elsevier BV and Copyright 2018 Nature Springer)

the signal obtained from objects in dark-field microscopy can be arbitrarily increased through higher incident light intensities. Lasers help in this endeavor as they provide much higher photon fluxes than traditional non-coherent light sources.

Compared to the signal generated by fluorescent probes, however, the scattered light from most nano-objects has very low intensities. According to Mie theory (Mie 1908; Wriedt 2012), the scattering amplitude, s, of a spherical particle (diameter < 1.6λ) scales (Baron and Willeke 2001) as:

$$s \sim \varepsilon_m \pi \frac{d^3}{2} \frac{\varepsilon_p - \varepsilon_m}{\varepsilon_p + 2\varepsilon_m} \tag{6.6}$$

where ε_p and ε_m are the dielectric constants of the particle and its surrounding medium, respectively, and d is the particle diameter. This means that the detected scattering signal of a particle decreases rapidly with its size. Following from the two Eqs. (6.5) and (6.6), a particle that reduces its diameter by half will only generate 1/64th of the signal.

Most organic matter intrinsically has a very similar dielectric constant to aqueous solutions, which additionally exacerbates the detection of single protein molecules using scattering as a contrast mechanism. Therefore, it is common to attach a marker to the molecule of interest that is made from a material with stronger polarizability.

Gold nanoparticles have become very popular as molecular probes due to their surface plasmon resonance effect. If gold particles are smaller than the wavelength of light, their electrons can be displaced within the gold lattice by the electric field such that a dipole is generated (Fig. 6.10a). The positively-charged ions in the lattice generate a restoring force making the electrons behave like a harmonic oscillator (localized surface plas-

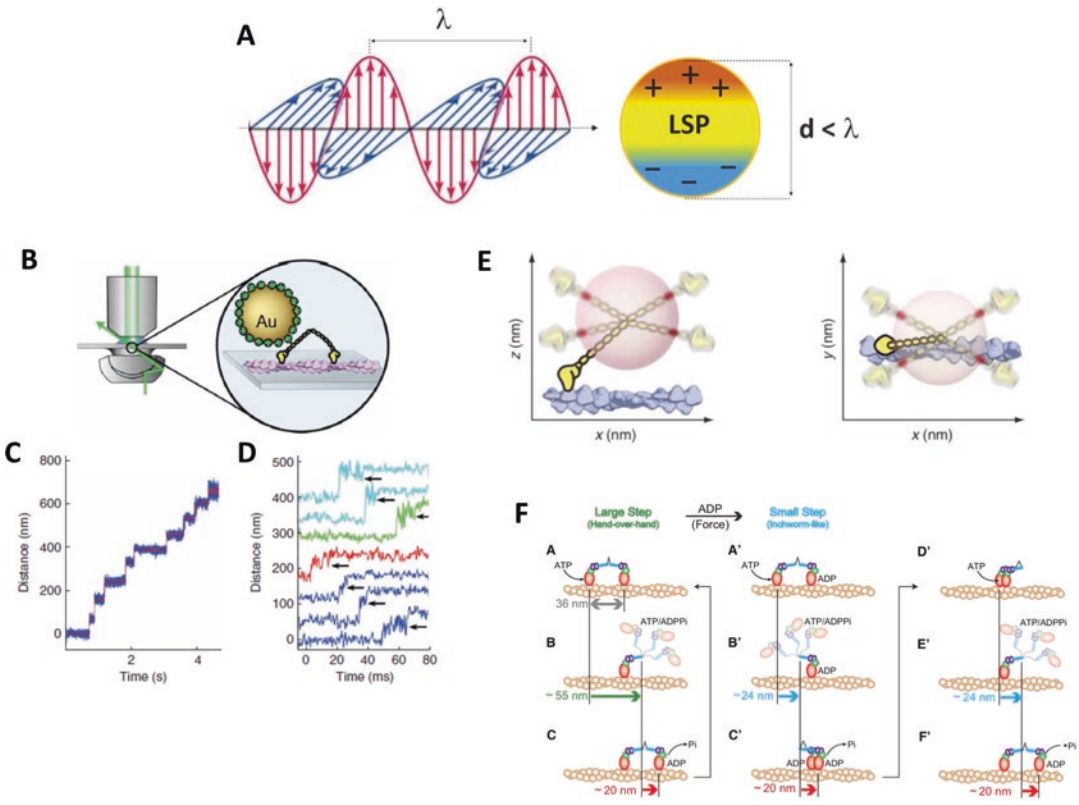

Fig. 6.10 Dark-field microscopy – Myosin-5a and myosin-6 experiments. (**a**) The electric field of light resonantly excites a localized surface plasmon (LSP) in a gold nanoparticle causing a strong scattering response. (Illustration from Amendola et al. 2017. Copyright 2017 IOP Publishing Ltd.) (**b**–**d**) Tracking the motion of the myosin-5 lever arm with millisecond time resolution. (**b**) A myosin-5 dimer is labeled with a gold nanoparticle on one of its lever arms through a biotin-streptavidin linkage. The myosin-5-gold conjugate walks along surface-immobilized actin. Light scattered by the gold particle is collected by the objective. (**c**) Sample data trace; 40 nm gold, 3 mM ATP. Frames were taken every 0.32 ms (blue); a 6.4 ms sliding average is shown in red. (**d**) Sample 49 nm substeps; 3125 Hz, 40 nm gold. The end of the substep is indicated by an arrow. Each color corresponds to an individual molecule. Note the increase in variance during the substep. (**e**) Dunn and Spudich swivel model how the observed increase in standard deviation for the gold location before each dwell can be explained. (Illustrations in **b**–**e** reproduced from Dunn and Spudich 2007. Copyright 2007 Nature Publishing Group). (**f**) Myosin-6 stepping model based on Qdot fluorescence and gold particle dark-field tracking experiment by the Yanagida laboratory. The myosin either steps in a hand-over-hand (left) or inchworm-like fashion (right). (Illustration from Nishikawa et al. 2010. Copyright 2010 Elsevier BV)

mon). The gold particles, therefore, act as "nano-antennas" with certain resonance frequencies, which depend on the surrounding medium and particle size, and they scatter light strongly at these frequencies (Amendola et al. 2017).

The strong scattering amplitude of gold particles has the additional advantage that their signal dominates over the background scattering in an aqueous sample and the species of interest can be equally well followed as a fluorescently-labelled molecule without any of the disadvantageous effects such as blinking and photobleaching that limit the achievable spatial and temporal resolution as discussed earlier.

The popularity of gold nanoparticles has led to the development of surface modification chemistry that enables the attachment of protein molecules to the gold particles. Thus, well-established biomolecular labelling methods for attaching the nanoparticles to the molecules of interest, such as through biotin-streptavidin or biotin/NeutrAvidin, are available.

Dunn and Spudich (Dunn and Spudich 2007) demonstrated the superiority of dark-field imag-

ing for the tracking of myosin motion in a study where they attached 40-nm gold particles to the lever arm of myosin-5 (Fig. 6.10b). Using this strategy, they could follow the conformational transitions of the motor during its processive runs at frame rates up to 3125 Hz, which enabled them to resolve the head motion in between the dwells on the actin filaments (Fig. 6.10c and d). They concluded that the detached head of myosin-5 freely pivots around the forward-leaning lever arm of the attached head before rebinding to the actin filament (Fig. 6.10e). They also noticed a lateral displacement of 4–8 nm of the detached head to the side of the actin filament axis (Fig. 6.10e), which they attributed to an off-axis contribution of the power stroke that could explain the observation that myosin-5 walks in a left-handed spiral (Ali et al. 2002). However, they argued that the size of the gold particle in this study could also have had a steric effect on the motor causing this displacement.

A similar study was conducted by Nishikawa and colleagues (Nishikawa et al. 2010) on myosin-6. They tracked 40 nm NeutrAvidin-coated gold particles attached to the biotinylated motor domain of an artificially dimerized myosin-6 construct with 2 nm localization precision at 37 μs time resolution. These experiments revealed a very distinct stepping behavior of the myosin in which the motor switches between a hand-over-hand and an inchworm-like mechanism. As the dark-field experiments allowed the observation of the detached state of the myosin head, the authors were able to determine the respective lever arm orientations during the two step types (Fig. 6.10f).

Even though dark-field microscopy appears to be a valuable alternative to fluorescence microscopy and provides a deeper mechanistic understanding of the studied molecular system, the technique has its limitations and pitfalls that should be mentioned here.

First of all, scattering-based measurements require a much more careful sample preparation as larger particles on the glass surface and in solution will have much greater impact on the background signatures than in fluorescence where the signal is specific to the labelled molecules.

As the above two examples show, it is possible to achieve nm spatial precision at μs temporal resolution with modern dark-field setups. In this time regime, however, the diffusional motion of the gold particle around its tether starts to be resolved and the ability to localize the myosin domain structure may be limited by this effect rather than by the localization precision for the gold itself. Therefore, it should be carefully considered what time scales are relevant for the chosen experiment and the average time window should be as long as possible when following a molecule's motion (Young and Kukura 2019).

A 40-nm gold particle is still a large marker compared to most fluorescent dyes (< 1 nm) or quantum dots (~10–20 nm), or even to the motor itself. This may reduce labelling efficiency or sterically interfere with the motor's conformational freedom. In order to minimally perturb the labelled protein, it would be desirable to use smaller nanoparticles or image entirely label-free. As discussed earlier, the strong scaling of the scattering signal with size makes it technically very challenging to achieve similar results with smaller nanoparticles.

Another scattering-based imaging technique called interferometric scattering microscopy circumvents the size scaling problem and enables high signal-to-noise, non-resonant imaging of smaller sized gold nanoparticles and even direct detection of native, unlabeled biomolecules.

6.5.2 Interferometric Scattering (iSCAT) Microscopy

If the goal is to image very small particles with a low scattering amplitude, pure scattering as a contrast mechanism quickly loses sensitivity. In this case, it is beneficial to include the background light that is rejected in dark-field microscopy. If we inspect Eq. (6.4) again, we find that the pure scattering term $|\mathbf{E}_s|^2$ becomes negligible for very small scatterers. However, the scattered light interferes with the background light and generates a signal defined by the third term $2|\mathbf{E}_r||\mathbf{E}_s|\cos\varphi$, which scales linearly with the par-

ticle volume and is therefore much more accessible than the pure scattering signal.

This principle has originally been realized by interference reflection microscopy (IRM) (Curtis 1964) or reflection interference contrast microscopy (RICM) (Ploem 1975). Its first biological application was to investigate the adhesion of cells to a glass substrate, because the technique proved useful to probe the optical path differences along membrane-water-glass interfaces (Curtis 1964; Limozin and Sengupta 2009). Later, less complex systems were chosen to enable more quantitative measurements (Rädler and Sackmann 1993; Rädler et al. 1995). These studies, however, did not achieve the signal-to-noise ratios required for nanoparticle detection. The advent of lasers finally enabled coherent illumination at much higher light intensities. A decade ago, the first laser-based setups, at this point called interferometric scattering (iSCAT) microscopes, were used to take non-fluorescent images of single quantum dots (Kukura et al. 2009a) and to track a virus particle diffusing on a lipid bilayer (Kukura et al. 2009b).

iSCAT's ability to track single particles with high spatial precision and temporal resolution makes it an ideal tool for myosin motility assays. A simple experimental setup is shown in Fig. 6.11a. A collimated laser beam from a diode laser is scanned over the sample by imaging a deflection from two orthogonal acousto-optic deflectors (AODs) producing a large, even illumination pattern. In order to separate the detection and illumination beam paths, a polarizing beam splitter (PBS) is used. It sends linearly polarized illumination through a quarter waveplate (QWP) and into the objective. The QWP circularly polarizes the light so upon reflection, the detected signal will be of an opposite handedness to the illumination and therefore converted by the QWP back into orthogonally linearly polarized light which is then reflected into the detection pathway by the PBS (Fig. 6.12). The image is captured by an sCMOS camera.

As with dark-field microscopy, myosin-5a was the first motor protein studied with iSCAT. The enhanced sensitivity of iSCAT makes it feasible to use smaller labels such as 20 nm gold nanoparticles, which minimize steric perturbation of the labeled motors. This allowed the Kukura group (Andrecka et al. 2015) to track 20 nm gold particles directly attached to the motor domain of myosin-5a without noticeably affecting its motion at 1 kHz frame rate and 4 nm localization precision (Fig. 6.11b–g). The reduced noise on the position of the detached head during myosin-5a's stepping cycle, compared to previous dark-field experiments, revealed that rather than undergoing a free 3D Brownian search, as suggested by the Dunn and Spudich study (Dunn and Spudich 2007), it occupies a spatially constrained state upon detachment of actin 40 nm off-axis and about 24 nm above the plane of actin. This result provided evidence that myosin-5 preserves the angle between its lever arms through structural constraints. It thereby reduces the degrees of freedom during its step which leads to a more directed and efficient 2-dimensionally constrained search for the next actin-binding site.

The study also observed a small rotation of the N-terminal part of the bound motor domain during its power stroke when the other head detaches. This is one of the only times a structural transition during the power stroke has been directly observed. The small rotation of the N-terminal domain during the power stroke, the constrained transient state of the unbound head together with results from a correlative fluorescence – iSCAT experiment (discussed later in this chapter) provide some interesting insight into how energy is transferred through myosin-5a's structure to lead to concerted, efficient, unidirectional motion.

A study by Ortega Arroyo and colleagues (Ortega Arroyo et al. 2014) has demonstrated that iSCAT-based imaging can even be used to visualize the motion of motor proteins without the need for external markers. Through careful removal of the static image background, the authors were able to extract the small scattering signal of native, single myosin-5a molecules (iSCAT contrast signal = 0.18%) and follow their movement along actin filaments in real time (Fig. 6.13a–e). The sensitivity was sufficiently high to reproduce the characteristic 37 nm step of the motor (Fig. 6.13e).

The sensitivity limit for label-free detection of proteins ultimately comes down to how much their signal can be raised above the measurement noise level. Assuming one can achieve purely

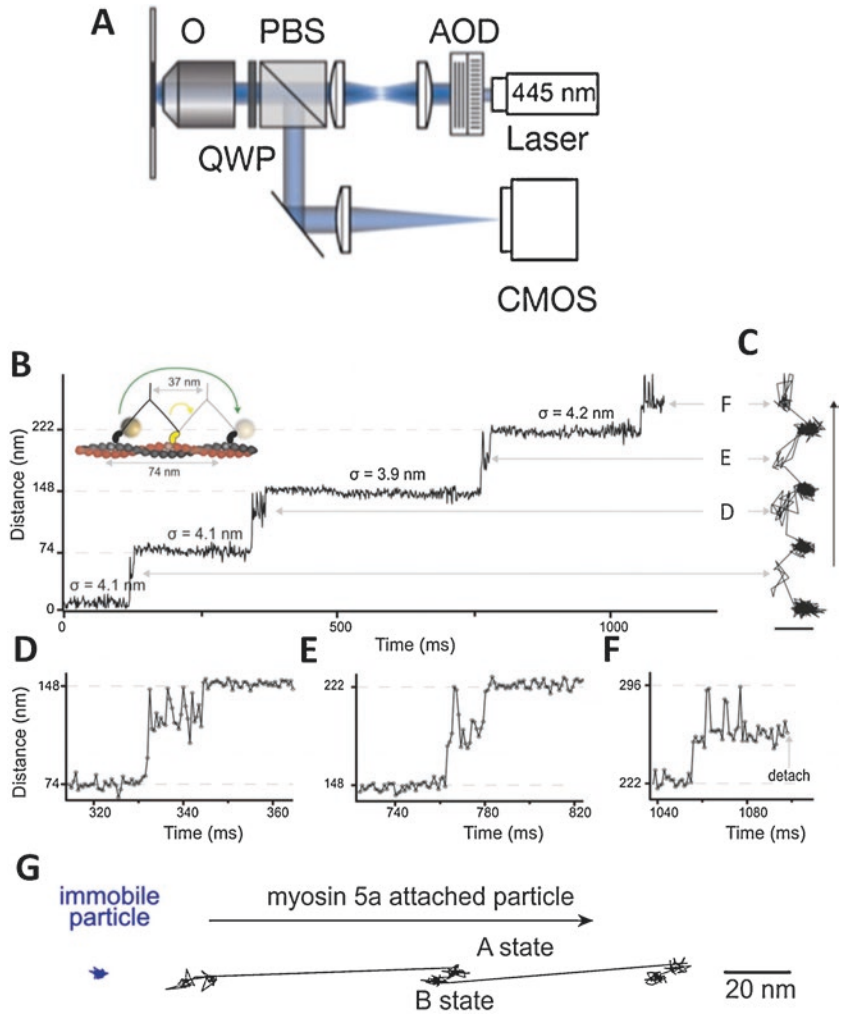

Fig. 6.11 iSCAT – Myosin-5a tracking. (**a**) Illustration of a simple iSCAT microscope. AOD = acousto-optical deflector, PBS = polarizing beam splitter, QWP = quarter-wave-plate, O = objective (Diagram reproduced from Ortega Arroyo et al. 2014.) (**b**–**g**) High-speed nanometric tracking of myosin-5 with iSCAT microscopy. (**b**) Distance traveled as a function of time for a single myosin-5 molecule biotinylated at the N-terminus and labeled with a 20 nm streptavidin-functionalized gold particle. The lateral localisation precision, σ, defined as the standard deviation of the positional fluctuations of the label while bound to actin is given above each of the actin-attached periods. Inset: schematic of gold-labeled myosin-5 stepping along actin. (**c**) Corresponding 2D-trajectory with the arrow indicating the direction of movement. (**d**–**f**) Close-up of the transient states indicated in B and C. ATP concentration: 10 μM. Scale bar: 50 nm. Imaging speed: 1000 frames/s. (**g**) Two states of the motor domain during myosin movement. Sample 2D trajectories for a 20 nm gold particle immobilised on the surface (left) and attached to the N-terminus of myosin-5a (right). The arrow indicates the direction of myosin movement. (Illustrations in B-G reproduced from Andrecka et al. 2015. Copyright 2015 eLife Science Publication)

shot-noise limited detection on a camera, which is possible using smart background removal strategies, the signal-to-noise ratio, (SNR), for a molecule is a function of its interferometric scattering contrast and the number of acquired photons, N.

$$\mathrm{SNR} = \frac{\text{iSCAT signal}}{\text{background fluctuations}} = \text{contrast}\sqrt{\mathrm{N}} \tag{6.7}$$

One strategy for improving the SNR is therefore to accumulate more photons from a sample,

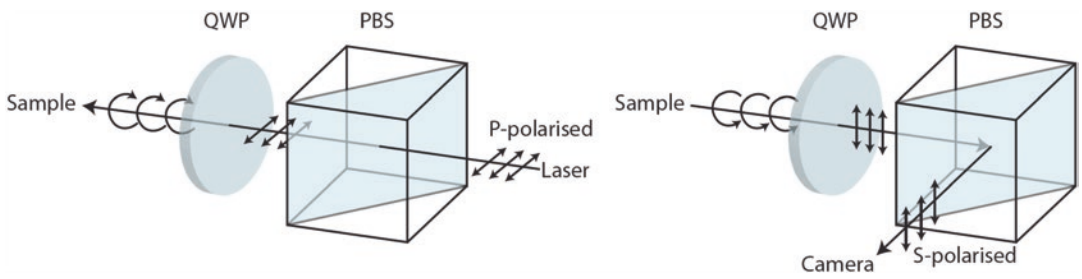

Fig. 6.12 Polarization-based separation of illuminating light from the detection path in iSCAT. (Top) S-polarized laser illumination is reflected by the polarizing beam splitter (PBS) and converted to circularly polarized light by the quarter waveplate (QWP). (Bottom) Reflected light from the sample returns with opposite handedness circularly polarised, is converted to p-polarized light by the QWP and transmitted by the PBS, effectively separating illumination and detection paths

i.e., measure at higher light intensities. Higher photon fluxes can be captured on cameras with high photon capacities and by distributing the signal over many frames and pixels. However, this approach has its limitations, especially because most cameras with high photon capacities have low quantum yields making them less efficient for collecting the incident light. It would require the detection of 10^8 photoelectrons to detect a signal that is 0.1% of the background illumination with an SNR of 10, but most cameras fail to provide a well capacity beyond 10^5 photoelectrons (Cole et al. 2017).

The alternative strategy would be to increase the contrast of a molecule while capturing the same number of photons. The iSCAT contrast of a particle is determined by the ratio between its signal, I_{det}, and the background intensity, I_{bkg}, which according to Eq. (6.4) is:

$$\begin{aligned}\text{contrast} &= \frac{I_{\text{det}}}{I_{bkg}} = \frac{|r|^2 + 2|r||s|\cos\varphi}{|r|^2} \\ &= 1 + \frac{2|s|\cos\varphi}{|r|},\end{aligned} \tag{6.8}$$

where $|r|^2$ is the reflectivity of the interface that provides the reference light. The contrast of a molecule can thus be increased by selectively reducing the amount of detected back-reflections from the sample. Technically, this is possible by making use of the fact that most of the signal from small scatterers is collected at high angles in the objective while the background light is evenly distributed over all angles of detection (typically the low numerical aperture of the objective) (Lee et al. 2011). By placing a partial reflective mirror into the back focal plane of the objective that attenuates the low numerical aperture contributions to the image, the contrast of scattering objects will be selectively enhanced (Cole et al. 2017; Liebel et al. 2017). This procedure does not by itself improve the SNR due to the concomitant loss of detected photons on the camera, but this can be compensated for by increasing the illumination intensity accordingly. The major advantage of this strategy is that by using the right combination of illumination intensity and reflectance of the mirror, cameras do not require extremely high well depths and the photons can be captured more efficiently. Figure 6.13f–h illustrates this approach schematically.

These recent technological advances in iSCAT microscopy have enabled high SNR, label-free imaging of proteins across most of the relevant size range. The ability to detect and accurately determine the interferometric contrast of individual proteins opens up another very exciting possibility. As most proteins have a very similar refractive index and specific volume, their contrast scales linearly with their mass (Piliarik and Sandoghdar 2014; Young et al. 2018). This can be used to generate mass spectra of protein samples in solution (Young et al. 2018). Since the contrast of each molecule can be determined very accurately, the size distributions obtained using this so-called mass photometry approach have better resolution than ensemble-based measurements

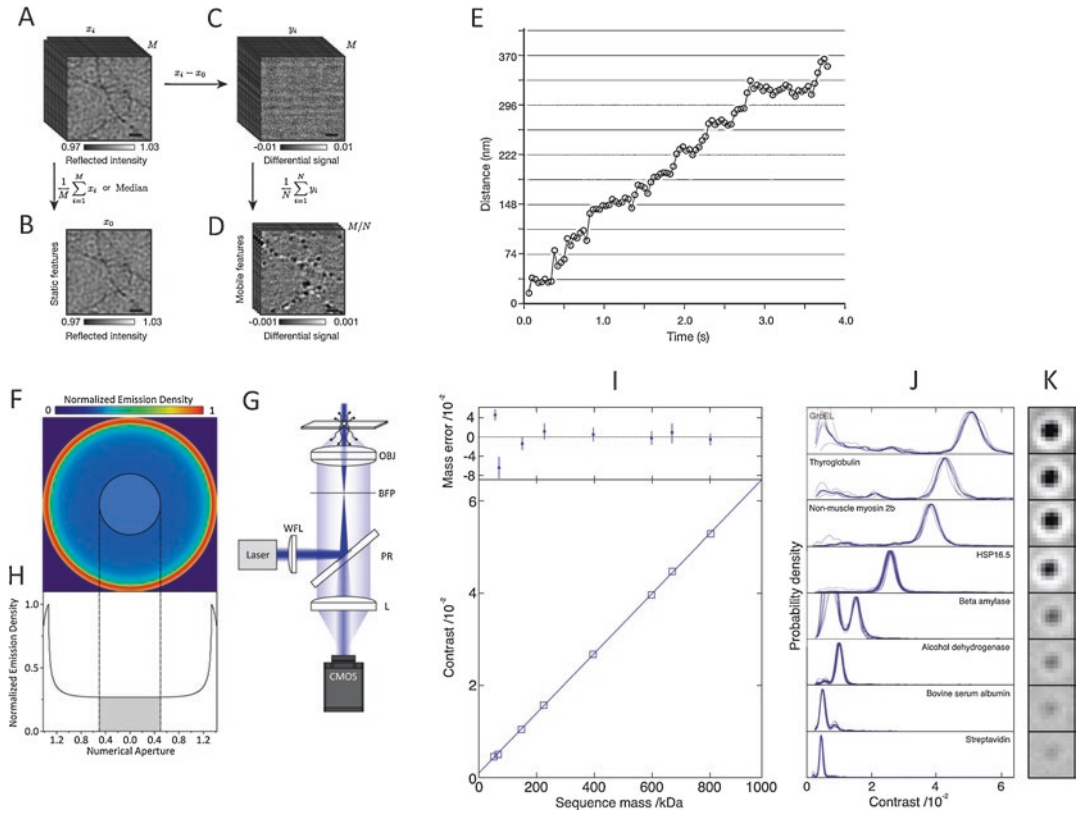

Fig. 6.13 Label-free iSCAT. (**a**–**d**) Interferometric scattering detection of myosin 5a HMM at the single-molecule level. (**a**) Sequence containing M iSCAT images, x_i, of actin filaments on a microscope cover glass in the presence of myosin-5a HMM. (**b**) An image containing purely stationary iSCAT features obtained by taking the median or averaging over the sequence of images in (**a**). (**c**) Sequence of M differential iSCAT images, y_i, obtained by subtracting the stationary iSCAT features from the image sequence in (**a**). (**d**) Time-averaged differential images generated by binning N = 170 consecutive frames together. Note the order-of-magnitude decrease in z-scale from (**c**) to (**d**). Scale bars: 1 μm (black line). (**e**) Distance traveled for a single myosin-5a molecule with contrast of 0.31% at 10 μM ATP concentration. Imaging speed: 1 kHz averaged to 25 Hz. (Illustrations in **a**–**e** reproduced from Ortega Arroyo et al. 2014. Copyright 2014 ACS Publication.) (**f**–**h**) Concept and experimental realization of numerical aperture filtered interferometric scattering microscopy (iSCAT). (**f**) Emission pattern of a nanoscopic scatterer at a glass−water interface emerging from the back aperture of a high-numerical-aperture (1.42) microscope objective for circularly polarized illumination. The semi-transparent circle indicates the region occupied by a partial reflector shown in the schematic experimental setup in **g** (**g**). Schematic of a numerical aperture-filtered iSCAT microscope. WFL = wide-field lens, BFP = back focal plane, OBJ = objective, PR = partial reflector, L = lens. (**h**) Emission density as a function of numerical aperture, with the gray area indicating the region attenuated by the partial reflector. (Illustrations in **f**–**h** reproduced from Cole et al. 2017. Copyright 2017 ACS Publication.) (**i**–**k**) Principle of iSCAT-based mass photometry. (**i**) Linear relationship between interferometric contrast and protein mass as determined using the standard proteins in **j** and **k**. (**j**) Size-distributions of the indicated standard proteins. (**k**) Exemplary point spread functions representing the protein peaks in **j**. (Diagrams in **i**–**k** modified from Young et al. 2018. Copyright 2018 Science)

like dynamic light scattering (DLS), size-exclusion chromatography (SEC) and analytical ultracentrifugation (AUC). Figure 6.13I-K illustrates this mass photometry approach, including the quality of data which can be achieved with this method.

Young et al. (2018) demonstrated that mass photometry can be used to investigate complex binding equilibria. In the future, the technique may therefore prove very useful to investigate the interaction of myosins with interaction partners, which has become a stronger effort in the field over the

past years. If mass sensitivity were combined with simultaneous single-particle tracking, iSCAT could become a very powerful tool for the investigation of reconstituted physiological myosin complexes and their motility entirely label-free.

6.6 Single-Molecule Force Measurements

6.6.1 Introduction

Considerable information about the functional principles of myosin motors has been extracted from single-molecule imaging methods. Only observing a motor, however, gives a superficial understanding of the way it works. The chemomechanical cycle of a myosin after all is designed to produce directed force that overcomes the random nature of processes in solution and facilitates coordinated motion in all living beings. A single myosin motor produces forces on the scale of pico-Newtons and displacements in the order of nanometers, but the sum of these small individual contributions can lead to macroscopic force production and displacements such as during muscle contraction.

If the goal is to understand the smallest components of a large-scale motor assembly on a molecular level and how force and motion are produced by its basic building blocks, it requires techniques that are sufficiently sensitive to detect pico-Newton forces and nanometer displacements that are able to interact with the motors under investigation.

The following sections will introduce a number of methods that have been employed in the myosin field to measure forces and displacements on a single-molecule level.

6.6.2 Glass Microneedles and ZnO Whisker Crystal Scanning Probe

The first force measurements of actomyosin interactions were performed using a thin glass microneedle (~300 nm in diameter) (Fig. 6.14a and b) made from a larger (1-mm diameter) glass rod. The needle-like extension was generated using a glass pipette puller (Kishino and Yanagida 1988) and had previously been used for microtubule sliding force measurements in flagella (Kamimura and Takahashi 1981). Biomolecules, such as actin or myosin, can be attached to the glass microneedle, and when an external force is applied, the microneedle will bend (Fig. 6.14a). Therefore, it can be used as a sensor for externally applied forces. The advantage of using a microneedle for force measurements is that it does not require any special optics, *i.e.,* microneedles can be combined with an existing microscope equipped with fluorescence optics. However, it does have its disadvantages, such as the fragility of the needles, and that every needle needs to be calibrated for use in force measurement. The time resolution achieved by using a microneedle can be up to ~1 ms by making it stiff and short (Ishijima et al. 1996), but drag forces imposed onto the needle make it inferior to other methods described later in this chapter.

Kishino and Yanagida (1988) measured the tensile strength of tetramethyl-rhodamine phalloidin-stabilized actin filaments (~110 pN), thin filaments (actin filaments decorated with tropomyosin and troponin) (~120 pN), as well as the force production by full-length rabbit skeletal muscle myosin-2 and the subfragment-1 (S1) actomyosin. They concluded that double-headed (*i.e.,* full-length) and single-headed proteins (*i.e.*, S1) generated ~0.2 pN force per head/motor domain. Note that these force values for individual motors were inferred from an ensemble experiment, whereby the force was measured with a microneedle attached to a single actin filament that was pulled by a "bed of myosins". The number of myosins attached to the surface in these studies was estimated based on the concentration used to coat the surface and used to calculate an "average" force from an individual molecule (Kishino and Yanagida 1988; Ishijima et al. 1991). A variation of the glass microneedle technique (Ishijima et al. 1994, 1996) was used later to probe single molecules of myosin-2 incorporated inside a "synthetic filament" composed of mostly tail domains of myosin-2.

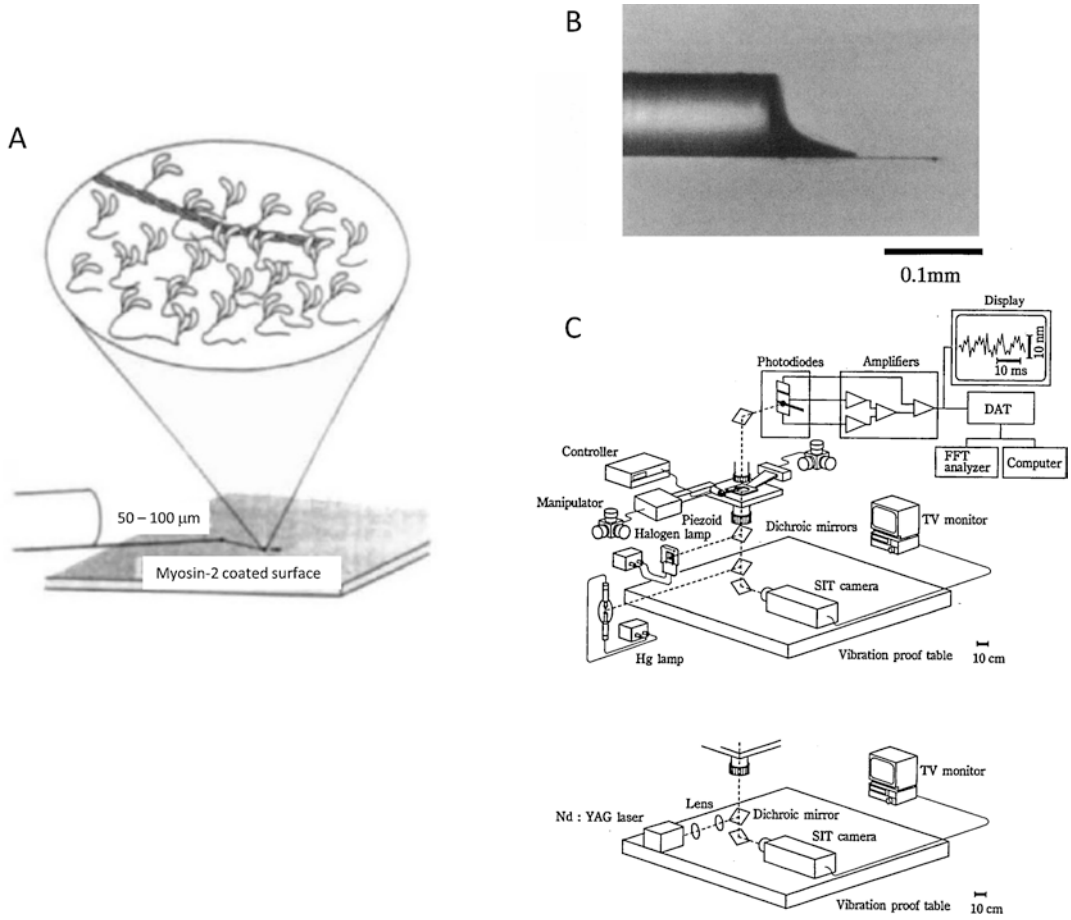

Fig. 6.14 Glass microneedle: actin and myosin-2. (**a**) Illustration of a glass microneedle assay. A single actin filament is attached to the end of the glass microneedle, ~50–100 μm long, and dragged along the myosin-2 coated surface. (**b**) Image of the glass microneedle using a dark-field microscope. (**c**) Schematic diagram of the high-resolution force and displacement measurement system using a microneedle transducer. (Diagrams reproduced from Ishijima et al. 1991, 1996. Copyright 1991 Nature Publishing Group and copyright 1996 Elsevier BV)

A zinc oxide (ZnO) crystal whisker scanning probe (Kitamura et al. 1999) was used as an improvement to the glass microneedle method, where a 5–7 μm long crystal with a 15 nm tip was used to attach a single S1 fragment of myosin-2 (Fig. 6.15). Rather than attaching an actin filament to a glass microneedle, actin was attached to a glass surface of an experimental chamber for this assay. This ZnO scanning probe instrument was also coupled to a TIRF microscope to allow a combination of force measurement using the ZnO scanning probe and fluorescence imaging to image the fluorescent myosin. The latter was used to ensure that the force measurements were taken with a single myosin on the tip. The study showed that a single S1 fragment of myosin-2 could take multiple, unidirectional, successive steps per actin encounter, varying from ~5 to ~30 nm, with an average step size of ~5.3 nm. These results indicated the possibility that the myosin head may be able to store energy from ATP hydrolysis and later release it productively in several packets of work. Measurements using an S1 fragment of myosin-5 was shown to behave similarly to make unidirectional, successive steps per actin encounter with an average step size of ~5.3 nm (Okada et al. 2007).

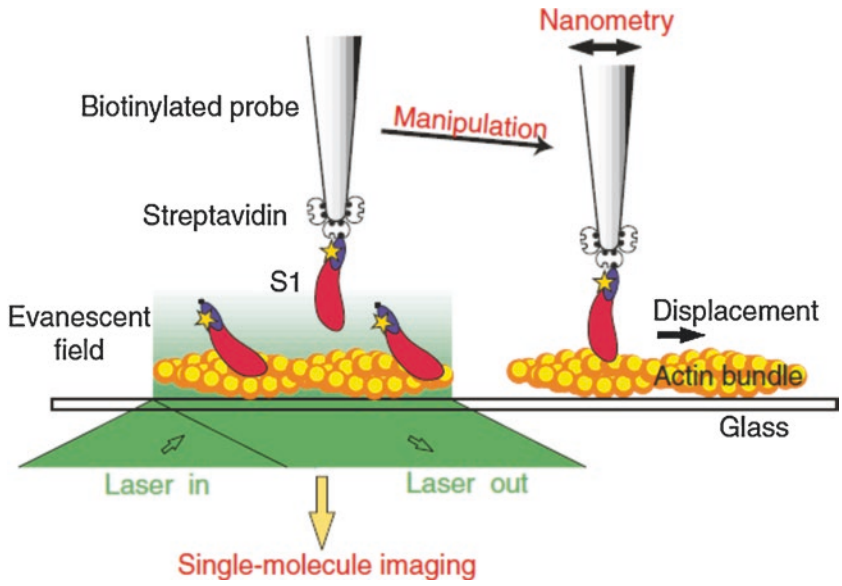

Fig. 6.15 ZnO whisker with myosin-2 subfragment-1 (S1) on tip. Scheme of the experiment is shown. A single myosin-2 S1 fragment, which was biotinlylated and labeled with a Cy3 dye, was attached to the tip of the ZnO whisker attached to a glass microneedle. Under TIRF illumination, the single myosin-2 S1 fragment can be manipulated onto the actin bundle while visualizing the Cy3 dye, and simultaneously, the ZnO whisker is used for nanometry to measure the force generation of a myosin-2 S1 in the presence of ATP. (Diagram reproduced from Kitamura et al. 1999. Copyright 1999 Nature Publishing Group.)

More details on the glass microneedle and ZnO crystal whisker scanning probe can be found in this methods article (Yanagida et al. 2011).

6.6.3 Atomic Force Microscopy

Atomic force microscopy (AFM) is another scanning probe microscopy method that has been used for decades for biophysical studies. AFM can be used for measuring forces and imaging molecules, as well as for manipulations.

In brief, AFM is dependent on the measurement of interactions between the sample surface and a probe, which is usually a thin tip. This tip is attached to a flexible cantilever that is bent as the tip interacts with the surface. There are different modes of how the tip can be used to probe. It can be brought into contact with the surface in order to sense a repelling force depending on the height of the surface. Alternatively, the tip can be held in close proximity and will experience attractive interactions. Another common method is to let the tip oscillate above the specimen. Detection of cantilever bending is detected via a laser focused onto the back of the cantilever and imaging the reflection of that laser beam on a photodiode. Changes in the position of the reflected laser beam on the photodiode are used to measure the interaction of the tip with the sample.

A basic scheme of an AFM is illustrated in Fig. 6.16 (Santos and Castanho 2004). The sample is attached to a piezo scanner, which can be moved at angstrom levels in order to generate an image of the surface topology at nm resolution. The AFM setup is usually coupled to an optical microscope for positioning the probe onto a field of interest.

As the bending of the cantilever is proportional to the interaction force between the tip and its substrate, the technique can also be used to measure forces. A traditional AFM detects forces between 10^{-7} and 10^{-12} N (Neuman and Nagy 2008).

The AFM is truly a useful method to measure forces of molecular interactions, however, due to the geometric constraints of how the AFM is set up with an optical microscope, it is hard to mea-

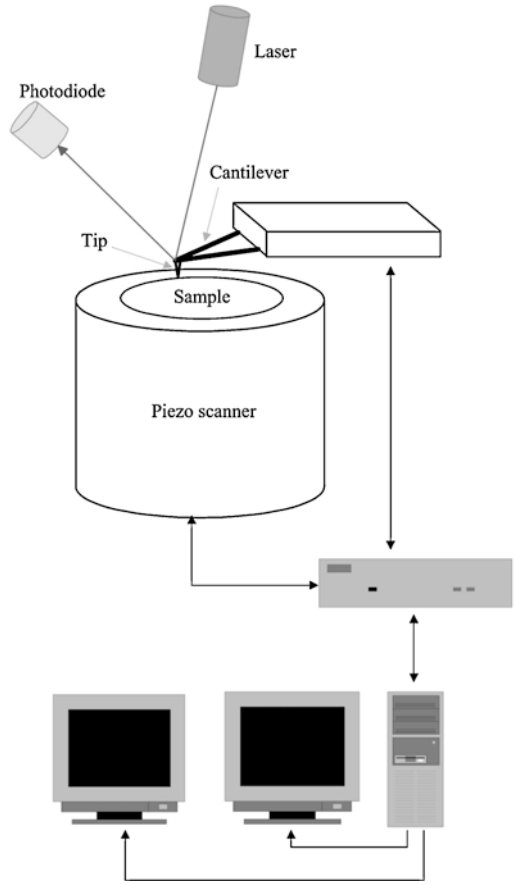

Fig. 6.16 Atomic force microscopy overview. A schematic representation of the components for an AFM setup. A cantilever with an "AFM tip" to probe the sample. Bending or twisting of the cantilever is detected by focusing a laser onto the cantilever face, opposite to the AFM tip. The reflection of the beam is focused onto a photodiode to detect forces in the range of 10^{-7} to 10^{-12} N. Scanning can be performed by moving the probe or the sample using a piezo-scanner, and usually with some variation of a feedback mechanism. Computer control is required for scanning as well as detection. (Diagram reproduced from Santos and Castanho 2004. Copyright 2004 Elsevier BV)

sure the mechanics or locomotion of a myosin. However, the method has been used to compare the elasticity of the tail domains of processive and non-processive myosin-5 at the single-molecule level (Nagy et al. 2009).

As mentioned above, an AFM can be used as a molecular imaging technique rather than for measuring forces between molecules. Technical advances in scanning speed and probing mechanism have led to the development of "high-speed" AFMs that achieve imaging speeds close to video rate. High-speed AFM has been used to directly observe single molecules of myosin-5 as they move on actin filaments, while actually resolving the structure of the protein (Kodera et al. 2010; Kodera and Ando 2018). The researchers in these studies were capable of visualizing myosin-5 translocation at ~7 frames-per-second (FPS) of a field-of-view (FOV) of ~100 × 100 nm^2, with a typical spatial resolution of ~2–3 nm in the lateral direction and ~0.15 nm in the vertical direction (Ando et al. 2013; Ando 2018). This incredible method, which is further discussed in Chap. 7 of this book, can be applied to studying many biomolecular systems, making it possible to directly watch motion and interactions at a molecular scale in action. It is a valuable tool that will surely be in the spotlight for many years in the single-molecule biophysics field (Ando 2014; Uchihashi and Scheuring 2018).

6.6.4 Optical Trap Measurements

The optical-trapping technique, invented by Arthur Ashkin in the mid 1970's, has been used widely in the biophysics field to study the detailed force-generating mechanism of molecular motors. Ashkin was one of three scientists who were awarded the 2018 Nobel prize in physics for creating groundbreaking tools from beams of light. Ashkin discovered that the momentum of light can be used as an extremely sensitive "trap" or "tweezers" to manipulate small particles.

Optical trapping started as "optical levitation" (Ashkin and Dziedzic 1975, 1985) whereby liquid droplets or particles could be trapped in air using the radiation pressure created by a laser beam. This is due to the fact that photons possess a momentum, p, that is dependent on their wavelength, and can be expressed as

$$|\vec{p}| = \frac{h}{\lambda}, \tag{6.9}$$

where h is the Planck constant. Thus, when a beam passes through a dielectric particle, such as a polystyrene bead with a refractive index (n) greater than the surrounding medium, it is

refracted away from the direction of the incident beam with a corresponding change in momentum of the laser. Due to conservation of momentum, there is an equal change in the momentum of the bead pointing into the opposite direction of the change in momentum of the laser beam. The momentum change leads to a force on the bead. The geometry of a laser focus is such that the net force on the particle directs it toward the center of the focus, where it will be trapped.

Another way to describe this effect is based on the particle's polarizability χ. The light's electric field induces an electric dipole moment $\boldsymbol{p}_{elec}$ in the particle, expressed as

$$\boldsymbol{p}_{elec} = \chi E \tag{6.10}$$

Thus, the force F on the particle in the electric field gradient of the light is

$$F = \boldsymbol{p}_{elec} \nabla E = \chi E \nabla E \tag{6.11}$$

This means that small particles will be drawn along the electric field intensity gradient, which pulls them into the focus of the beam. By focusing a beam of light to a diffraction limited spot, *i.e.,* with a high numerical aperture objective lens, one can create a large electric field gradient to effectively immobilize the particles.

Eventually, Ashkin found that this method could also be used to optically "trap" a dielectric particle in three dimensions in water (Ashkin et al. 1986). Following this finding, he published numerous papers putting forth the elementary steps to using optical traps as a quantitative tool to measure biological mechanics and kinetics. He first showed that the optical trapping technique could be applied to the trapping of viruses and bacteria (Ashkin and Dziedzic 1987) using a spatially filtered argon laser (wavelength = 5145 Å). He then changed the wavelength of the laser to an infra-red regime (1.06 μm neodymium-doped yttrium aluminum garnet, Nd:YAG) to minimize optical damage to live specimens and showed that the technique could be used to trap cells such as yeast and red blood cells (Ashkin et al. 1986) without altering their growth rate (for yeast), or flexibility and shape (for red blood cells). Furthermore, Ashkin showed that organelles inside the plant cytoplasm (Ashkin and Dziedzic 1989), as well as in amoebae (Ashkin et al. 1990), could be trapped to perform "laser surgery" to pick up structures inside cells or to measure escape forces of organelles/mitochondria that were suspected to move via microtubule-based motors, such as kinesin and dynein. An illustration of the early custom-made optical-trapping setup is shown as Fig. 6.17.

Apart from these cell-based applications, optical trapping allows for the manipulation of particles such as polystyrene or silica beads, which can be used as handles for proteins or other molecules. Unlike the microneedle transducer explained previously, the optical trap provides more freedom to manipulate these particles giving versatility to the assay geometry. Furthermore, the trapped particle with biomolecules attached exerts substantially lower drag force than the long microneedle due to the smaller particle size (*i.e.* 1 μm polystyrene beads).

While optical traps are useful as tools for the micromanipulation of small objects, they can be used as a very sensitive force sensor, too. At its simplest description, the optical trap functions as a very weak Hookean spring, which confines a particle within its three-dimensional potential well. The force F exerted on a displaced particle according to Hook's law is

$$F = -k \cdot x, \tag{6.12}$$

where k is the spring constant/optical trap stiffness and x is the displacement of the particle from the center of the optical trap. The force exerted on the trapped particle can be directly measured through its displacement if the trap stiffness is known. It is worth noting that this relationship only works for small distances from the trap center (~200–300 nm). Usually, either the bead image or the laser scattered by the trapped bead is monitored using a quadrant photo diode (Visscher et al. 1996) (Fig. 6.18).

6.6.4.1 Optical Trap Force Calibration

As the trap stiffness, k, depends on many different parameters like the objective's numerical aperture, the wavelength of the laser, the laser intensity and the refractive indices of particle and medium, its value is usually determined

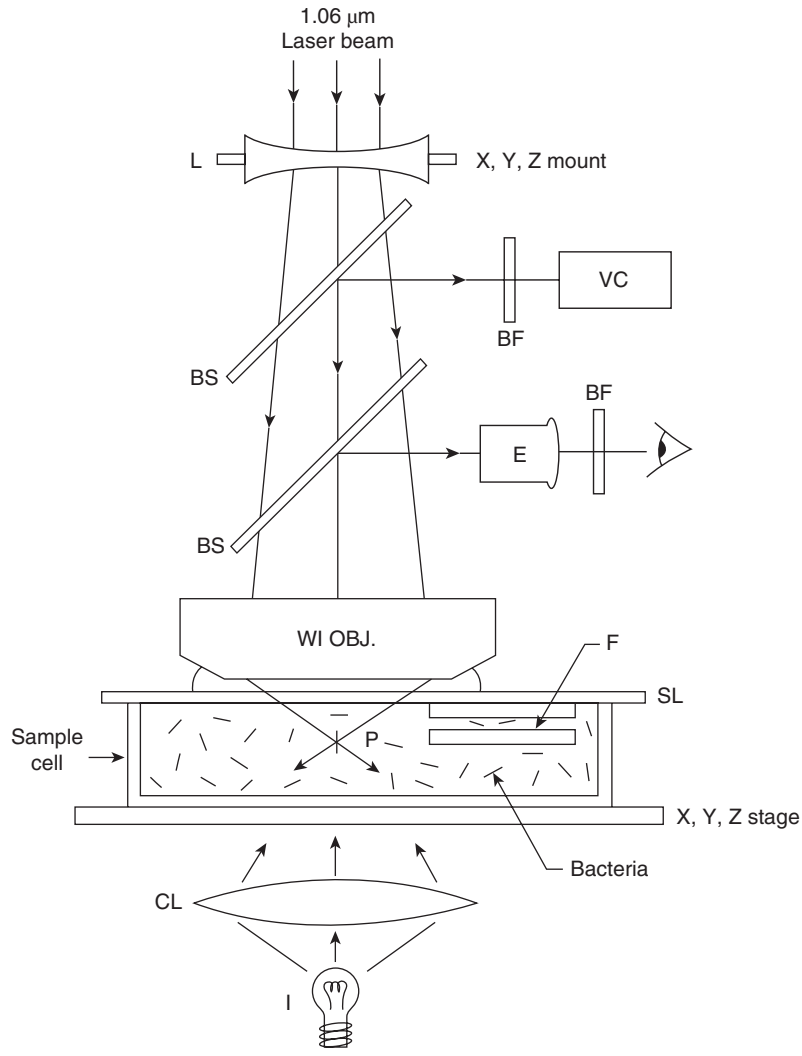

Fig. 6.17 Optical trapping overview. A schematic diagram of the combined high-resolution optical microscope and 1.06 mm infra-red laser trap for observing, manipulating and separating bacteria and other organisms. L = lens; BS = beam splitter; WI OBJ = 1.25 N.A. water immersion objective lens; CL = condenser lens. I = illuminator; E = eye piece; VC = video camera; P = trapping beam focused at point P. (Diagram reproduced from Ashkin et al. 1987. Copyright 1987 Nature Publishing Group)

empirically for a given particle/trap specimen. This procedure is referred to as a force calibration.

The simplest way of calculating the trap stiffness from a sample record of the statistical position fluctuations of a bead in a trap works through considering the equipartition theorem (Neuman and Block 2004), which predicts that the translational freedom of a particle in one dimension based on thermal fluctuations is $\frac{1}{2}k_bT$, where k_b is the Boltzmann constant and T is the absolute temperature. Without external perturbations, a bead in an optical trap will therefore fluctuate within the spring potential $\frac{1}{2}\, k < x^2 >$ up to values of $\frac{1}{2}k_bT$.

$$\frac{1}{2}kx^2 = \frac{1}{2}k_bT \tag{6.13}$$

$$\Leftrightarrow k = \frac{k_bT}{x^2} \tag{6.14}$$

The trap stiffness k can thus be directly calculated from the bead's mean squared displacement $<x^2>$. The disadvantage of this simple method is that the value of the trap stiffness depends on the accuracy of the displacement measurements, which are themselves determined through a calibration. Moreover, additional noise sources (e.g., localization noise, read noise from the position detector, drift) contribute to the value of $<x^2>$ and lead to an underestimation of the trap stiffness.

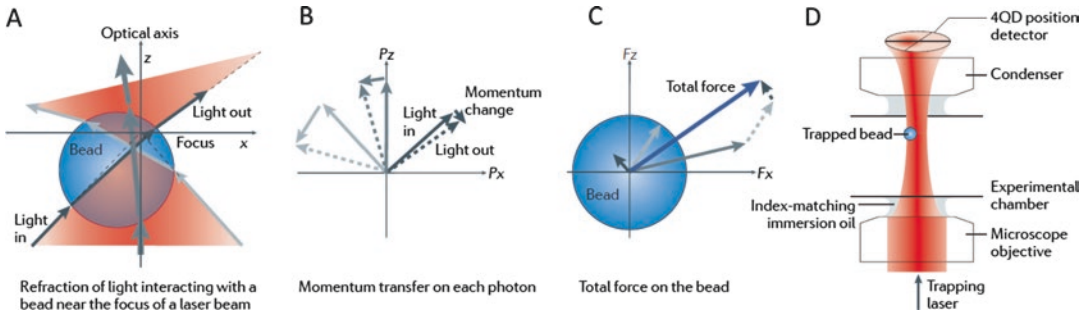

Fig. 6.18 Optical trapping ray diagrams and detection. (**a**) Ray optics sketch of light rays within a focused laser light illustrated in a red gradient. The laser is refracted through the bead that is trapped showing the three different gray light paths. The width of the gray arrows indicates the strength of the light intensity, which is highest through the optical axis. (**b**) Deflection of each photon results in a momentum change and a transfer of that momentum onto the bead. The arrows between the original photon momentum (solid lines) and the deflected photon momentum (dashed lines) illustrate the momentum transfer for each photon. (**c**) The total momentum transfer over time on all deflected photons from the three rays equals the force exerted onto the bead, shown in blue. (**d**) Position and force detection by back-focal-plane interferometry using a quadrant photodiode (4QD) placed after the microscope condenser so that it collects the deflected laser light and detects angular shifts in the transmitted trapping light. (Diagram reproduced from Veigel and Schmidt 2011. Copyright 2011 Nature Publishing Group)

Due to these shortcomings, it has become more common to determine the trap stiffness using the power spectrum of a bead's position fluctuations (Visscher et al. 1996; Gittes and Schmidt 1998; Neuman and Block 2004). This method does not require absolute position values to determine the trap stiffness. The Fourier transform or power-spectrum of the position fluctuations of an optically trapped bead usually shows a flat distribution at low frequencies (Fig. 6.19), which reflects the particle's restricted motion in the focused laser beam. The particle is not restricted by the trap at high frequencies resulting in an exponential decay of the power spectrum as usual for a freely diffusing particle (Fig. 6.19). This behavior is commonly described with a Lorentzian function.

$$S(f) = \frac{D}{\pi^2 \left(f_c^2 + f^2\right)}, \tag{6.15}$$

where $D = k_bT/\gamma$ is the diffusion coefficient for a spherical particle with the drag coefficient $\gamma = 6\pi\eta r$, the viscosity of the surrounding liquid, η, and the radius of the particle, r. The cut-off frequency (also called corner or roll-off frequency), f_c, is a characteristic frequency that describes where the spectrum drops off and depends on the trap stiffness, k, in the following way:

$$f_c = \frac{k}{2\pi\gamma} \tag{6.16}$$

The cut-off frequency, and thus the trap stiffness, can be determined by fitting the Lorentzian in Eq. (6.15) to an experimental power spectrum of the bead/trap combination that is meant to be calibrated.

The Lorentzian in Eq. (6.15) is an approximation that only holds when the sampling rate of the detection system is considerably higher than the cut-off frequency of the trapped bead, which ensures that the power spectrum can be determined reliably over a sufficient spectral frequency range. This may not be fulfilled when operating at high trap stiffness and the simple Lorentzian will systematically underestimate the cut-off frequency and thus the trap stiffness. Berg-Sørensen and Flyvbjerg (2004) have introduced an improved expression for the power spectrum that takes into account the frequency dependence of viscous drag on the particle and the effects of the sampling frequency and signal filtering during acquisition on the resulting experimental power spectrum. They provide a MATLAB routine that can be used to fit data

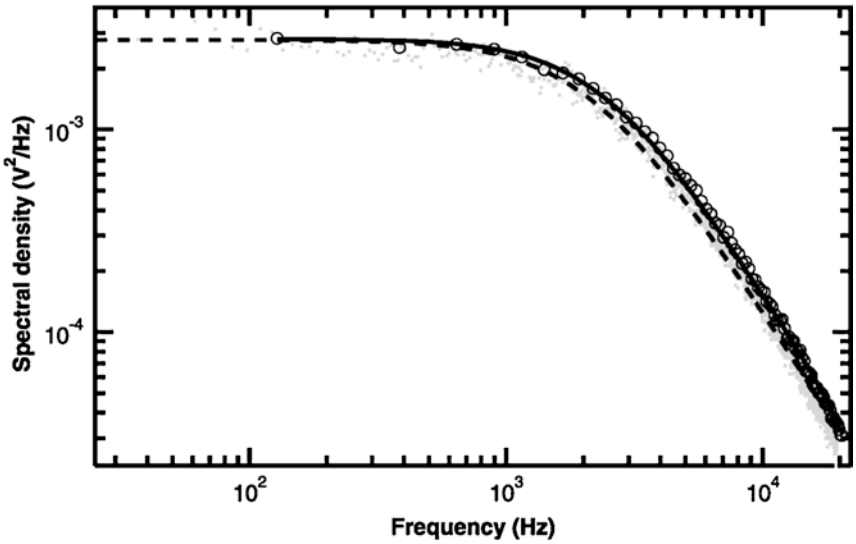

Fig. 6.19 Optical trap calibration. Power spectrum of a trapped bead. Power spectrum of a 0.5 μm polystyrene bead trapped 1.2 μm above the surface of the trapping chamber recorded with a position-sensitive detector (gray dots). The raw power spectrum was averaged over 256-Hz windows on the frequency axis (black circles) and fit (black line) to a Lorentzian function [Eq. (6.15)] corrected for the effects of the antialiasing filter, frequency-dependent hydrodynamic effects, and finite sampling frequency, as described by Berg-Sørensen and Flyvbjerg 2004. The cut-off frequency is 2.43 kHz, corresponding to a stiffness of 0.08 pN/nm. For comparison, the raw power spectrum was fit to an uncorrected Lorentzian function (dashed line), which returns a cut-off frequency of 2.17 kHz. Whereas the discrepancies are on the order 10% for a relatively weak trap, they generally become more important at higher cut-off frequencies. (Diagram reproduced from Neuman and Block 2004. Copyright 2004 AIP Publishing)

based on these more complicated considerations (Hansen et al. 2006). Figure 6.19 shows a comparison between a power spectrum fitted with a simple Lorentzian and the optimized routine. This method in general provides a more accurate estimate of the trap stiffness and has been implemented by more laboratories in the field in recent years.

6.6.4.2 Single-Bead Assay

In the late 1980's/early 1990's, the "bead motility" assay described earlier in this chapter was used to study the processive motion of single kinesin motors with an optical trap (Block et al. 1990; Svoboda et al. 1993). The concentration of the kinesin was titrated down to a regime where beads were very rarely bound with a single kinesin. This "single-bead" optical trapping assay (Fig. 6.20a) allowed the characterization of bead motion in an optical trap, such that the measurement was an output of the kinesin motion and force (Svoboda et al. 1993; Coppin et al. 1996). The kinesin attached to the bead was brought into close proximity of the microtubule and allowed to bind, then take multiple catalytic steps against the force of the optical trap until it either detached or stalled under force. These early experiments showed that kinesin is a processive motor that takes ~8 nm steps on microtubules. For myosins, it was not until the late 1990's/early 2000's that the single-bead optical trapping assay was used to characterize the mechanics and kinetics of myosin-5 (Rief et al. 2000), which was the first of the processive myosins to be discovered in 1993 (Cheney et al. 1993).

This single-bead assay to study the mechanics and kinetics of a processive molecular motor, such as kinesin, was useful since at least one of the motor domains of a processive motor is always attached to the track during its translocation process. However, this assay does not work well for non-processive motors, which briefly detach from the track. In the beginning, when optical trapping was used for myosins in the early

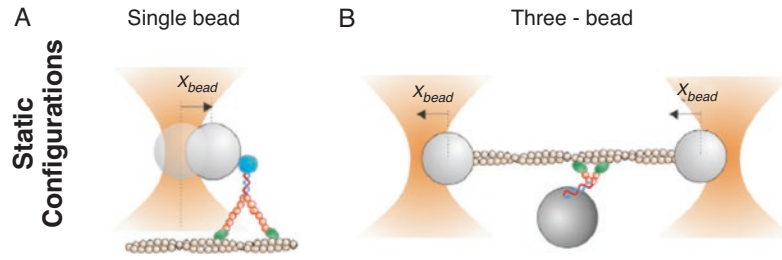

Fig. 6.20 Single-bead and three-bead assay schemes. (**a**) In a single-bead/trap configuration, the trap is static and the bead displacement, shown as X_{bead}, allows measurement of the molecular motor moving against the trap along a surface-bound track. If the optical trap force is higher than the stall force of the molecular motor, the protein will detach from the track and return back towards the center position of the trap. The single-bead configuration is useful for determining the mechanics of processive molecular motors. (**b**) In a three-bead assay, both optical traps are static with a track such as an actin filament in tension attached between the two beads. The molecular motor will exert motion against the track to displace the beads either closer to or further away, by X_{bead}, from the center of the trap due to the direction of force generation. The three-bead assay can be used to study the mechanics of both processive and non-processive molecular motors. (Diagram reproduced from Capitanio and Pavone 2013. Copyright 2013 Elsevier BV)

1990's, the only type of myosins discovered were non-processive ones. In order to study these non-processive myosins, a new geometry for the optical trapping assay needed to be developed.

6.6.4.3 Three-Bead Assay

Historically, for single-molecule actomyosin interactions, the "three-bead" assay (Finer et al. 1994; Molloy et al. 1995; Guilford et al. 1997) was developed to study the interactions, i.e., the power stroke and forces of non-processive myosins (Fig. 6.20b). Since non-processive myosins, such as skeletal muscle myosin-2 (Finer et al. 1994; Molloy et al. 1995; Guilford et al. 1997) or smooth muscle myosin-2 (Guilford et al. 1997; Lauzon et al. 1998; Tanaka et al. 2008), briefly detach from the actin filament every time they go through their enzymatic cycle, it would not be possible to use the single-bead assay (Block et al. 1990) as for processive motors, which can take multiple catalytic steps while at least one motor domain stays attached to the track. To overcome this limitation, the three-bead assay positioned the actin filament, suspended between two optically-trapped beads (a so-called actin filament "dumbbell"), above a third, usually larger, surface-bound bead sparsely coated with myosin used as a pedestal. In this geometry, when the myosin undergoes its enzymatic cycle and detaches briefly from the actin filament, the filament will remain in close proximity to the myosin such that it will quickly find the actin filament again. Data collection therefore becomes easy since many attachment/detachment processes of non-processive actomyosin interactions can be monitored within a short period of time. Parameters such as the size of the power stroke and the dwell/attachment times of unitary actomyosin interactions can be measured using this technique (Knight et al. 2001). Many studies have used the three-bead assay to measure the mechanics and kinetics of processive myosins as well (Mehta et al. 1999; Moore et al. 2001; Rock et al. 2001; Veigel et al. 2002, 2005; Purcell et al. 2005; Kad et al. 2008; Norstrom et al. 2010; Sellers and Veigel 2010; Watanabe et al. 2010; Takagi et al. 2014; Hundt et al. 2016; Gardini et al. 2018).

6.6.4.4 Load-Dependent Mechanics and Kinetics Using the Three-Bead Assay

Another beneficial attribute of the optical trap assay is that a load can be applied to the studied molecule in a controlled manner. Accordingly, measurements of how the kinetics of the motor's conformational transitions are altered by external force, or load, can be directly examined. Most optical trapping experiments are performed using a low stiffness (~0.01–0.03 pN/nm), so that the

displacement caused by an actomyosin interaction is measured under low load. This also greatly increases the signal-to-noise ratio of the detached *versus* the attached states of the actomyosin interactions, facilitating the separation of these states based on the variance or co-variance of the bead position signals.

In one variation of the experiment, the load on the myosin is altered using a "dynamic feedback" once an interaction between the myosin and actin filament is detected. This can be achieved by a fast change in laser power, which changes the trap stiffness, or by moving the actin filament with respect to the myosin.

Initial experiments using a dynamic feedback consisted of increasing and decreasing the laser power to mimic a situation whereby the myosin is undergoing a near-isometric condition (Finer et al. 1994; Molloy et al. 1995). An isometric condition in a single-molecule assay is one in which the relative positions, or strain, of single interacting myosin and actin molecules remain fixed by maintaining the position of one of the beads in a fixed position to reduce its motion. These methods revealed a distribution of isometric forces between 1–7 pN, with peaks centered around 2–3 pN.

Soon after these initial experiments, it was apparent that the end-compliance of the bead-actin attachments for the dumbbell assembly was highly non-linear (Dupuis et al. 1997; Mehta et al. 1997; Veigel et al. 1998) in the range of forces (~2 pN) previously applied. The problem with the three-bead assay is that if there is insufficient tension on the bead-actin connections in the dumbbell, the bead displacements and forces measured can be large underestimates of the actual displacements and forces produced by the molecular motor because some of the myosin motion is damped by the actin-bead-link compliance. Studies were performed to determine the connection stiffness of the bead-actin linkages by either looking at the limited correlated diffusion between motion of the two optically-trapped beads attached to the ends of a single actin filament (Mehta et al. 1997), or by moving one of the positions of the bead via the optical trap controlled by an electro-optical device (Dupuis et al. 1997; Veigel et al. 1998). From these experiments, it was determined that for the three-bead assay, it should be a routine to apply 4–6 pN of tension to the dumbbell to minimize measurement errors.

The method for determining the actin-bead link stiffness was also used to perform measurements on the stiffness of the actomyosin cross-bridge (Veigel et al. 1998). By driving one optical trap in a large-sinusoidal wave while keeping the other bead stationary (Fig. 6.21), it was possible to disentangle the stiffness of the myosin-actin link from that of the actin-bead connections. This way, crossbridge stiffnesses for single actin-myosin-2 interactions have been determined in the range of 1–2 pN/nm (Smith et al. 2001; Capitanio et al. 2006; Takagi et al. 2006; Lewalle et al. 2008). The method has also been used to determine the stiffness of other myosins such as myosin-5a (Veigel et al. 2002) and myosin-10 (Takagi et al. 2014).

Consequently, application of oscillations to the dumbbell complex in the three-bead assay has been a useful technique to also decrease the temporal limitation of detecting events (Veigel et al. 1998, 1999; Sellers and Veigel 2010; Nagy et al. 2013; Takagi et al. 2014; Hundt et al. 2016). The detection strategy of events, as described briefly earlier in this section, was based on the difference in thermal fluctuations between the detached and attached states. An initial attempt of this oscillatory method was a procedure using a small amplitude, 1 kHz sine wave onto one of the traps with an AOD to artificially increase the positional noise, or variance, which can then be detected at the other sensor bead. Due to the larger signal variance created, the relative decrease in the variance when the myosin attached to the actin filament was more pronounced and easier to detect. Using this method, binding events were therefore detected within ~1 ms. Furthermore, in combination with this oscillatory technique, a range of assisting and resisting loads was applied to a unitary actomyosin interaction within ~3 ms after detecting a binding event. This technique created a new avenue for both detection and load application using the three-bead assay in the studies of many myosins (Veigel et al. 1999). In recent

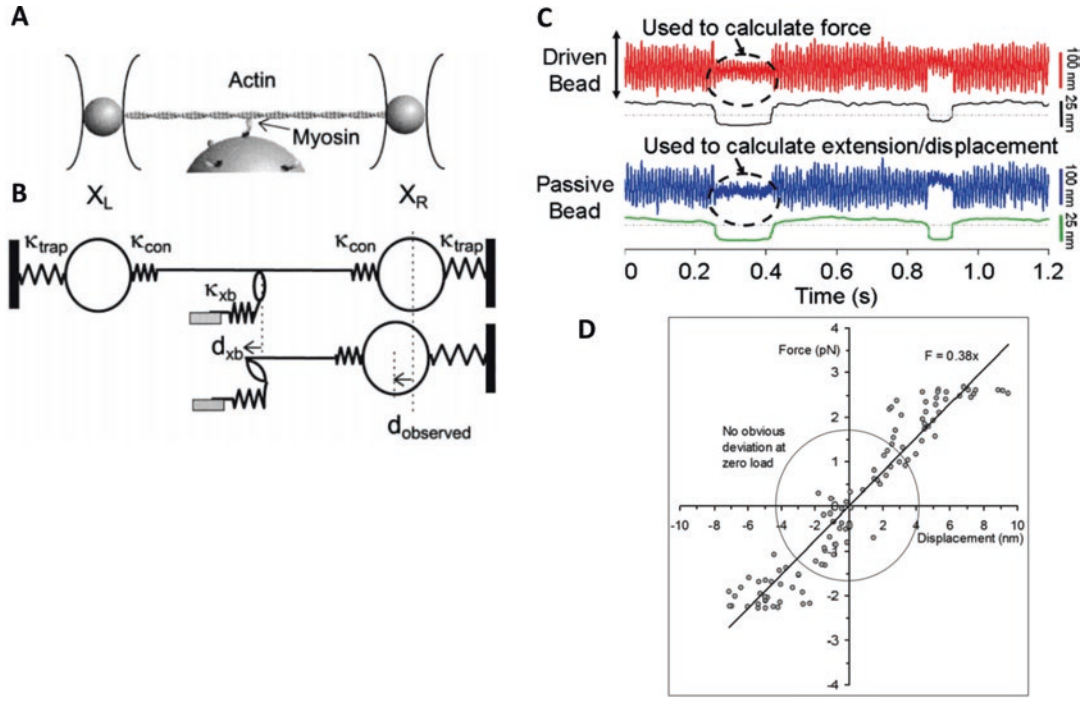

Fig. 6.21 Measuring the myosin stiffness using the three-bead assay. (**a**) The three-bead geometry scheme shown allows the manipulation of a taut actin filament strung between two optically-trapped beads to be positioned over the myosin, which is attached on a third larger bead on the surface of an experimental chamber. In this scheme, the position of the two beads, X_R and X_L, are monitored using a quadrant photodiode/detector. The three-bead geometry can be represented as a system of springs and masses, i.e., a mechanical system, as shown in (**b**). When a myosin attaches to the actin, the cross-bridge stiffness, κ_{xb}, is in series with the actin-to-bead connection stiffness, κ_{con}. These springs are also in parallel with the optical trap stiffness, κ_{trap}. The actual cross-bridge power stroke, d_{xb}, depending on the stiffness of these different springs, can be taken up by their compliance, and thus, the bead displacement observed (d_{obs}) could be an underestimate of the actual power stroke. A mechanical system allows interpretation of how the system reacts to different external loads, displacements and stiffnesses and can be a useful method to understand the mechanics of the three-bead assay. (**c**) The stiffness of a myosin-10 was measured using the output of the two quadrant photodiodes monitoring the two different optical traps. A large amplitude triangular wave (100 nm; 10 Hz) was applied to drive one of the optically-trapped beads back and forth, while simultaneously measuring the bead position at both ends of the actin filament. The difference in position between the bead held in the driven trap and the trap centroid was used to calculate the applied force, while the position of the bead on the other end of the actin filament allowed distortion of the acto-myosin-10 complex. Following a mathematical correction for the actin-bead connection compliance, force-extension diagrams were plotted. Force extension data in (**d**) show a stiffness of ~0.38 pN/nm for a single acto-myosin-10 complex. (Diagram reproduced from Veigel et al. 1998 and Takagi et al. 2014. Copyright 1998 Elsevier BV and copyright 2014 National Academy of Sciences, USA)

years, this method has been used to show that non-muscle myosin-2A requires a resisting load to be an efficient processive motor (Hundt et al. 2016), showing predominantly 5 nm forward steps and stall forces of ~4 pN.

As a variation of the three-bead assay with oscillations, a recently developed method called "**H**armonic **F**orce **S**pectroscopy" (HFS) (Sung et al. 2015) automatically and randomly applies sinusoidally varying loads to a single actomyosin interaction by moving the dumbbell complex with respect to the stage when attached to the myosin (Fig. 6.22). Published methods of harmonic force spectroscopy have applied sinusoids with an amplitude of 30–50 nm and frequencies between 100 and 200 Hz using a piezo-electric stage, while the actin dumbbell undergoes cycles of myosin binding and unbinding. Force-

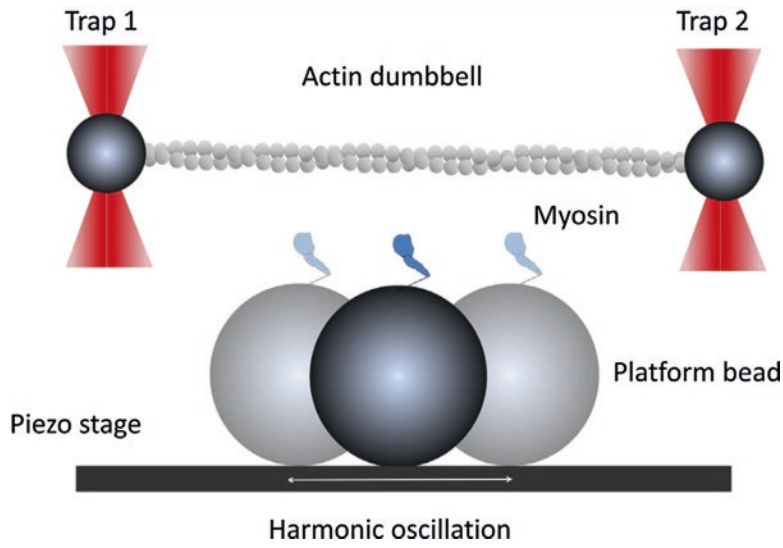

Fig. 6.22 Harmonic force spectroscopy (HFS). Using a standard, static, three-bead assay in concert with a simple harmonic oscillation introduced by the piezo-stage, HFS can be used to measure the load-dependent kinetics of molecular motor interactions without intricate feedback loops. (Diagram reproduced from Sung et al. 2017. Copyright 2017 Elsevier BV)

dependent kinetics of many β-cardiac myosin-2 mutation constructs have been studied in the past few years using this method (Liu et al. 2018). This technique appears to be a very useful variation to the three-bead assay, whereby this method also can be incorporated by moving the dumbbell complex using an electro-optical device, rather than the stage.

Innovative methods to incorporate a feedback system into the three-bead assay in order to decrease the end-compliance and to apply forces in different directions relative to the power stroke of the myosin have been developed over the years. In the previously described methods for measuring isometric forces, the actin filament moved significantly, and due to the limited tension applied to the dumbbell, the isometric forces measured were most likely an underestimate. To decrease the end-compliance, as well as to measure the isometric force, a feedback system that includes the whole dumbbell component in the feedback was developed (Takagi et al. 2006). In this feedback mode, an approach was taken to reduce and adjust the extent of actin motion at the moment of myosin binding. This method incorporated a procedure where one of the beads in the dumbbell was fixed in force by using an AOD while changing the position of the other bead. In this manner, the effective stiffness of the trap is increased, enabling testing of the effect of the stiffness on the developed force (Fig. 6.23b). The results showed that the force developed by unitary skeletal muscle actomyosin-2 interactions is considerably increased when the dynamic stiffness of the actin presented to the myosin molecules is increased. The authors showed that using this feedback mode, termed "isometric force clamp", the rate of load application can be altered, as fast as in the range of milliseconds or slower. Using a high gain feedback with a reaction time to apply dynamic load within ~1 ms, myosin-2 was shown to produce a range of forces between 2.5 pN and 17 pN with an average of ~6 pN, which was significantly higher than the earlier estimates in the 1–4 pN range (Finer et al. 1994; Molloy et al. 1995; Guilford et al. 1997). This single-molecule measurement of skeletal muscle myosin-2 force seems compatible with high-resolution muscle fiber measurements, which reported an estimate of ~6 pN per actomyosin crossbridge (Piazzesi et al. 2007).

Application of this method has also revealed novel features of myosin-1. In the presence of small loads, ~2 pN, the detachment of this myosin from actin filaments decreases by >75-fold, demonstrating that myosin-1 can transition from a low (<0.2) to a high (>0.9) duty ratio motor, supporting the motor's role as a molecular force sensor (Laakso et al. 2008). Furthermore, load-dependent kinetics differences within different

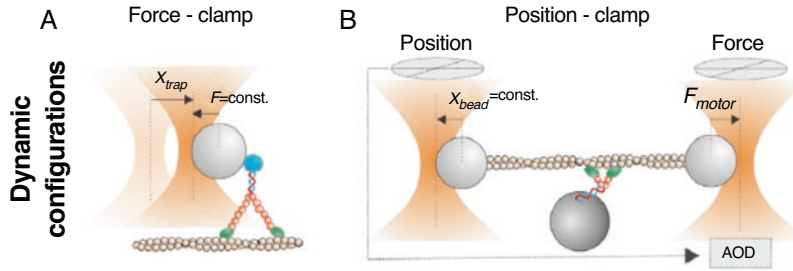

Fig. 6.23 Optical trapping feedback schemes. (**a**) Using a single-bead trapping geometry, a force clamp can be performed. In this case, a feedback loop is used to move the optical trap and keep the force on the trapped bead constant. The trap displacement, X_{trap}, measures the molecular motor motion under a force clamp. (**b**) A position clamp, also known as the isometric clamp, is performed by using the left bead as a "sensor" bead to detect the movement of the dumbbell and moving the right bead using an AOD to oppose the detected motion of the sensor bead, keeping it at its pre-determined position. The right bead therefore measures the actual force, F_{motor}, output by the molecular motor under isometric condition. (Diagram reproduced from Capitanio and Pavone 2013. Copyright 2013 Elsevier BV)

myosin-1 isoforms have been studied (Greenberg et al. 2012) as well as the role of the N-terminal domain in this load-dependence behavior of myosin-1s (Greenberg et al. 2015).

To measure force-dependent actomyosin kinetics and mechanics even faster than ~1 ms time resolution as achieved by the previously mentioned methods, ultrafast force-clamp spectroscopy has been used to apply constant loads with only a delay of ~10 μs (Capitanio et al. 2012; Capitanio and Pavone 2013). This system utilizes two separate AOD-driven feedbacks, one for each optical trap, to force-clamp the two beads at two different forces. Thus, within this feedback, a net constant force of +ΔF is applied to the dumbbell assembly, where the clamped force for one of the beads is −F, and the other F + ΔF. Different from previous methods, the dumbbell therefore moves against viscous drag at a constant velocity when the actin filament is not attached to the myosin, and by altering the direction of the net force, the dumbbell complex can move in a triangular wave, of ~+/−200 nm. Since the ultrafast force clamp is supposed to maintain the force between the dumbbell complex in the absence and presence of an attachment, the constant force of +ΔF is transferred to the myosin when it attaches to the actin, with a concomitant "stop" of the dumbbell movement (Fig. 6.24). Using this method, the Capitanio group showed that under resistive loads, ~5–10 nm power strokes usually followed binding after a short dwell time (0.2–1 ms). However, particularly short events (< 1 ms) did not exhibit any substantial power stroke. Furthermore, using a detailed analysis on the effect of applied load, a premature (< 5 ms) dissociation pathway was shown to be more populated as the force was increased, resulting in a working stroke that decreased with amount of load.

6.7 Simultaneous Methods

Some of the single-molecule methods described in this chapter have been combined to measure multiple parameters of myosin output, simultaneously. A couple of these attempts, which used a combination of different single-molecule techniques, are discussed as examples.

6.7.1 Optical Trapping and Fluorescence

The strengths of displacement and force measurements using optical trapping has been coupled to a single-molecule fluorescence detection scheme to visualize the nucleotide occupancy relative to motion of a single myosin (Ishijima

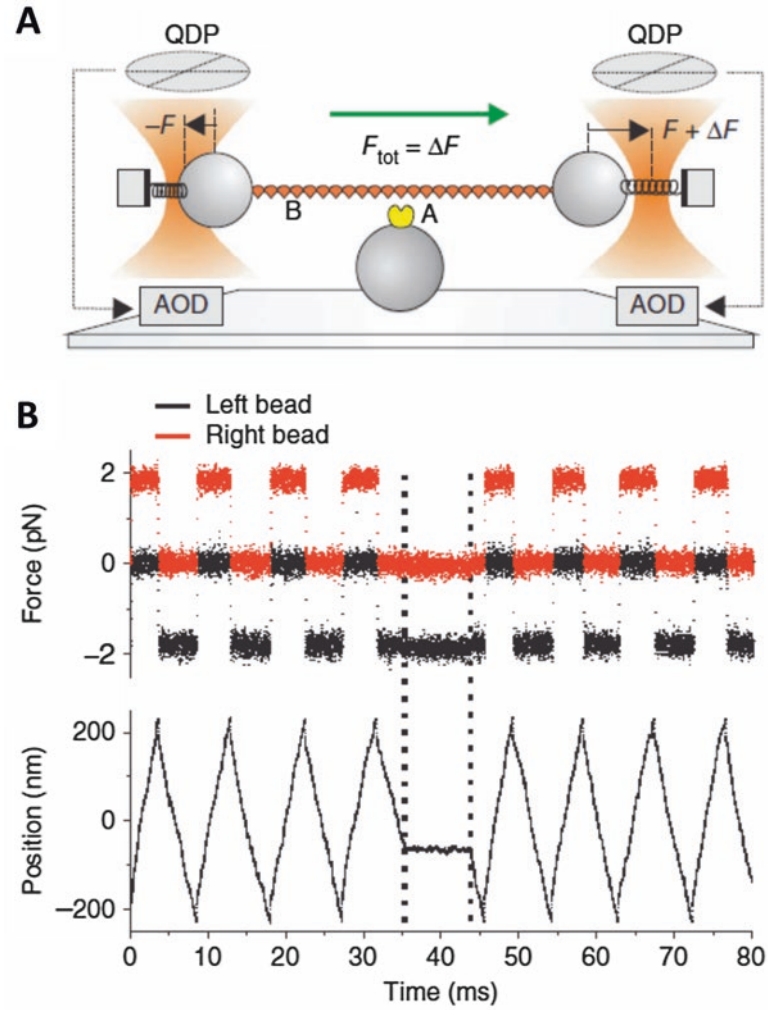

Fig. 6.24 Ultrafast force-clamp spectroscopy overview. (**a**) Schematic of the ultrafast force clamp spectroscopy relies on using two separate feedback systems to apply -F on the left optical trap and $F + \Delta F$ on the right optical trap such that molecule B, i.e., an actin filament, is under a total force of ΔF. Feedback operates on monitoring the force using a quadrant detector photodiodes (QDP), while moving the optical traps with an acousto-optic deflector (AOD). (**b**) Illustration of ΔF on the left (black) and right (red) beads. Within the ultrafast force-clamp feedback, the force is switched back and forth between $+\Delta F$ and $-\Delta F$ so that the bead-actin-bead complex oscillates within a confined distance of ±200 nm. When molecule A binds to B, the constant force is transferred to B, stopping the dumbbell motion as illustrated between the dotted black lines. (Diagram reproduced from Capitanio et al. 2012. Copyright 2012 Nature Publishing Group)

et al. 1998). This *tour de force* article coupled an optical trapping microscope capable of performing a modified three-bead assay together with a TIRF microscope (Fig. 6.25). In order to visualize a uniform TIRF image, glass surfaces were chemically etched to microfabricate "flat" pedestals that were ~ 7 μm wide and 1 μm deep. This study measured the force and displacement of a unitary, single-headed skeletal muscle myosin-2, while simultaneously observing a fluorescent nucleotide (Cy3-ATP) colocalized near the point of the acto-myosin interaction. Cy5 dyes were also used to visualize the actin filament within the three-bead assay, as well as the artificial thick filament made with a 1:1000 ratio of single-headed skeletal muscle myosin-2:skeletal muscle

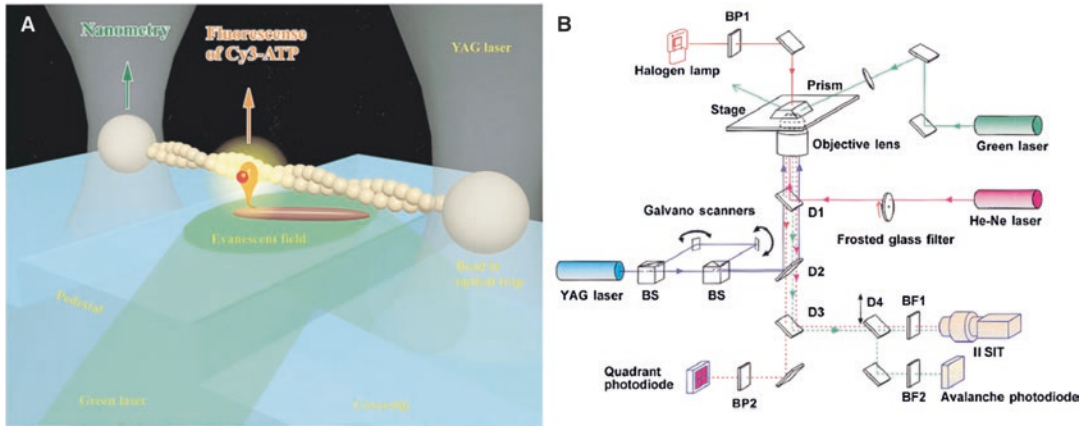

Fig. 6.25 Simultaneous optical trap/TIRF microscopy scheme. (**a**) Illustration of the assay at the specimen plane. Using a three-bead assay geometry an actin filament was brought into contact with a synthetic single-headed myosin-rod co-filament (myosin: rod ratio = 1:1000) attached to a pedestal microfabricated on the surface of the coverslip. TIRF microscopy was used to visualize Cy3-ATP as it associates and dissociates while the myosin undergoes its enzymatic cycle. (**b**) Optics layout of the optical trap/TIRF microscope. D = dichroic lenses; BS = beam splitter; BF = barrier filter; BP = band pass filters; II SIT = image intensified silicon intensifier target camera. More details can be found in the original article. (Diagram reproduced from Ishijima et al. 1998. Copyright 1998 Nature Publishing Group)

myosin-2 rods. This strategy of labeling both the actin filament and the synthetic co-filament of myosin-2 and rods, made controlling the angle of contact between the two individual filaments possible (~30°). This was done because previous studies had suggested that forces and displacements were strongly dependent on the angle between an actin filament and the myosin (Ishijima et al. 1994; Tanaka et al. 1998).

Interestingly, these measurements showed that force generation can happen several hundred milliseconds after the release of ADP from the myosin head, as if the myosin has a prolonged hysteresis or memory effect. This was an unusual finding which does not seem to fit any of the conventional kinetic mechanisms for myosin. Since nobody else has performed these simultaneous optical trapping and fluorescence measurements for myosins, it would be interesting to see if others obtain similar results in the future, and whether similar effects are observed with other classes of myosins.

6.7.2 Single-Molecule Fluorescence and iSCAT

A fluorescence channel has also been coupled into an iSCAT experiment in order to visualize two domains of myosin motors simultaneously. This, in practice, is a relatively simple modification in which a dichroic mirror is added into the illumination pathway. A blue laser is focused through a 500 mm lens into the back focal plane of the objective steered by two adjustable mirrors. The beam position can be displaced laterally by mounting one of the mirrors onto a translation stage in order to switch between epi-illumination and TIRF. Another dichroic mirror will separate the red-shifted emission from the illumination channel, and the image is passed through a filter and is focused onto an EMCCD. By using a red wavelength for the iSCAT channel, a fluorescence detection window in the green region can be used, ideal for molecules labelled with GFP. Using standard experimental techniques,

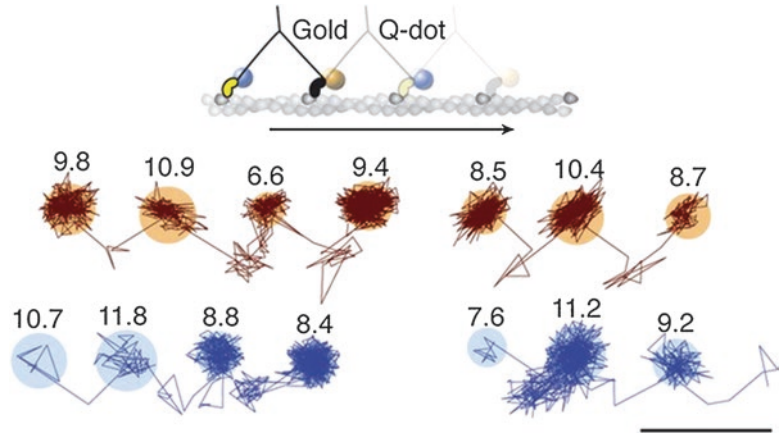

Fig. 6.26 Simultaneous iSCAT/TIRF microscopy of myosin-5a. One head was labeled with a 20 nm streptavidin-functionalized gold particle (red) and the other with a fluorescent quantum dot (blue). Reported values correspond to the standard deviation, σ, in the position of the bound state (nm) and the shaded regions encompass an area of 3σ. The traces are colored according to the label colors in the inset. ATP concentration: 10 μM. Scale bar: 100 nm. Imaging speed: 500 frames/s. (Diagram reproduced from Andrecka et al. 2015. Copyright 2015 eLife Science Publication)

the two channels can be temporally synchronized and spatially registered in order to achieve two truly correlated images.

This technique has been used effectively by the Kukura laboratory (Andrecka et al. 2015) to further understand the structural motion of myosin-5a (Fig. 6.26). Similar to the dual Qdot labeling strategy (Warshaw et al. 2005) employed previously for SHREC, they labelled both motor domains, one with a gold nanoparticle for scattering imaging and one with a Qdot for fluorescence imaging. Andrecka et al. observed that the spatially constrained transient state of the motor domain (discussed in detail in Chap. 8 in this book) occurred on the same side of the actin. This was the first evidence for a spinning compass-like gait of myosin-5a. This gait model would suggest that the cargo of myosin-5a should also rotate with each stride, or that some swivel in the myosin's structure alleviates the torsional strain that would be generated. Such a rotation has been measured before by the orientation of quantum rods attached to the myosin-5a tail, although in this work the source of the rotational movement was thought to be thermal (Ohmachi et al. 2012). The compass-like spinning motion may be an indication of how myosin-5a's structure helps facilitate and control the motion of the unbound head in a 1-dimensional arc to achieve a high specificity in finding the desired binding site, aiding unidirectional motion.

Andrecka et al. also simultaneously tracked one myosin-5a motor domain with the stalk domain. The motor domain was labelled with a gold nanoparticle and a C-terminal GFP was conjugated with a GFP booster nanobody as reported in Ries et al. 2012. The results showed that both the translocation of labeled motor domain and the small rotation of the N-terminus on the bound motor domain (again, discussed in more detail in Chap. 8) occurs synchronously with the translocation of the stalk. This provides evidence that the small-scale N-terminus transition observed is representative of the pre- to post-power stroke transition, a process previously unobserved. These experiments show that simultaneous observation of scattering and fluorescence can be a useful method to track the different domains of a molecular motor, facilitating understanding of how motions of different domains are coupled to each other.

6.8 Commercially Available Microscopes/Parts from Companies

Implementing single-molecule techniques into a laboratory with no previous background on the subject is a difficult and demanding task. The field is often very technology-driven. It therefore helps to understand and follow the trends and information relevant to single-molecule techniques in order to be innovative. However, single-molecule techniques are just a set of tools that can be used to answer the right question, if set in the right context.

The fact that many microscopes and instruments are commercially available these days helps newcomers to implement single-molecule measurements into their research. In this section, we list a number of companies and information (available in 2019) about "where to start" if one were interested in learning more about commercially available systems. Only a subset of existing companies is listed in this section.

Commercial Microscope Companies: Rather than building a microscope from scratch, it is sometimes beneficial to use a platform that already has a variety of imaging modalities built-in. The more established and well-known microscope companies have a variety of different types of microscopes that can be used to custom-build an instrument specific to your single-molecule investigations and needs. Furthermore, many of these companies also have "turn-key" solutions for single-molecule studies – for example, TIRF microscopes capable of single-molecule detection that have both hardware and software already pieced together to work effectively. Additionally, discussions with the application scientists and engineers from these companies with a thorough background and understanding of different microscopy techniques is a great way to learn about what types of microscope platforms are available from each company and which may be suitable for the single-molecule experiments one would like to perform.

Leica: https://www.leica-microsystems.com/
Nikon: https://www.microscope.healthcare.nikon.com/Products
Olympus: https://www.olympus-lifescience.com/en/
Zeiss: https://www.zeiss.com/microscopy/us/solutions/life-sciences.html

Single Molecule Microscope Frames: If one chooses to build a microscope from scratch, there are companies such as Edmund Optics, (https://www.edmundoptics.com/), Newport (https://www.newport.com/), OptoSigma (https://america.optosigma.com/?redirect_to=optosigma_us) and Thorlabs (https://www.thorlabs.com/) that sell both optics and opto-mechanical parts. An alternative is to start with a versatile microscope frame as a scaffold that can be modified according to the user's needs. These are usually compatible with other off-the-shelf components offered from the companies, making it possible to assemble a microscope like a LEGO-set.

Applied Scientific Instrumentation (ASI) - RAPID AUTOMATED MODULAR MICROSCOPE SYSTEM (RAMM): http://www.asiimaging.com/products/complete-system-solutions/rapid-automated-modular-microscope-ramm-system/
Mad City Labs - RM21™: http://www.madcitylabs.com/singlemolecule.html
Sigma Koki - Core Unit for Microscopy: https://www.global-optosigma.com/en_jp/Catalogs/pno/?from=page&pnoname=CUMS-GUIDE&ccode=&dcode=

Single Molecule Fluorescence Imaging: Companies, such Oxford Nanoimaging, also have built-in turn-key solutions to many types of single-molecule fluorescence techniques. The system called Nanoimager can be configured to perform single-molecule fluorescence imaging and single-molecule fluorescence resonance energy transfer (smFRET) microscopy. In addition, the system has imaging modalities that can be used for super-resolution imaging of cells, such as PALM, direct STORM, and structured illumination microscopy (SIM). The hardware system from Oxford Nanoimaging is packaged with data acquisition software, as well as a suite of analysis software.

Oxford Nanoimaging (ONI): https://oni.bio/

Interferometric Scattering Microscopy: For scattering-based single-molecule techniques such as iSCAT microscopy, Refeyn Ltd. has a turn-key system (Refeyn One^{MP}) that is capable of interferometric scattering mass photometry measurements. For dark-field scattering experiments, many of the large microscope companies provide dark-field condensers which are commercially available for their microscopes.

Refeyn Ltd.: https://www.refeyn.com/

Optical Trapping: A number of companies exists that provide commercial units specific for optical trapping. Some are fully integrated units, some are components that can be used to bolt onto existing microscopes, and some are modular kits that can be built to your specific optical-trapping needs.

Elliott Scientific: https://www.elliotscientific.com/Optical-Tweezers
IMPETUX: https://www.impetux.com/
JPK/Bruker: https://www.jpk.com/products/force-sensing-optical-tweezers-and-optical-trapping
LOT-QuantumDesign GmbH: https://lot-qd.de/en/products/life-sciences/optical-tweezers/product/optical-tweezers/
Lumicks: https://lumicks.com/
Meadowlark Optics: https://www.meadowlark.com/optical-tweezers-cube-p-120?mid=12
Molecular Machines & Industries (MMI): http://www.molecular-machines.com/single_cell_sorting_products/mmi_cellmanipulator_-_optical_tweezers/technology_55
Thorlabs Inc.: https://www.thorlabs.com/newgrouppage9.cfm?objectgroup_id=12442 or https://www.thorlabs.com/newgrouppage9.cfm?objectgroup_id=3959 or https://www.thorlabs.com/newgrouppage9.cfm?objectgroup_ID=6966

AFM: Atomic force microscopes are also commercially available. Some come as stand-alone units, and some can be attached/combined to a light microscope for simultaneous imaging modes.

JPK/Bruker: https://www.jpk.com/products/atomic-force-microscopy
Nanosurf: https://www.nanosurf.com/en/
Oxford Instruments/Asylum Research: https://afm.oxinst.com/
Research Institute of Biomolecule Metrology Co., Ltd. (RIBM): https://www.ribm.co.jp/

6.9 Conclusion

In this chapter, we discuss some of the single-molecule techniques that have been used to study myosins over the last three decades. Single-molecule techniques are truly advantageous tools that make it possible to decipher the molecular mechanisms of enzymatic activity and directed force production by molecular motors that cannot be easily assessed with ensemble techniques.

Many questions about different types of myosins have been challenged and answered using single-molecule approaches with considerable agreement among many laboratories. However, at the moment there is also considerable disagreement in the field concerning many of the myosins. Perhaps further enhancement of both the temporal and spatial resolution, as well as new ways of studying external parameters, such as load, with these single-molecule techniques may help resolve some of these experimental differences. Other single-molecule techniques such as magnetic tweezers (Seol and Neuman 2018), which have been used to study other molecular motors, but which have not been used to study myosins, may pave new avenues of myosin research and advance our understanding about these well-studied, yet still mysterious, molecular motors.

Acknowledgements We thank Dr. James R. Sellers (NHLBI, NIH) for critical reading of the chapter, as well as for helpful discussions and ideas. Y.T. was supported by the intramural funds from the NHLBI, NIH (Grant HL 004229). N.H. was supported by a DFG (German Research Foundation) research fellowship (HU 2462/1-1) and later by a DFG return grant (HU2462/3-1). A.F. was supported by a ERC starting investigator grant (nanoscope, 337757).

References

Aksel T, Choe Y, Sutton S, Ruppel KM, Spudich JA (2015) Ensemble force changes that result from human cardiac myosin mutations and a small-molecule effector. Cell Rep 11(6):910–920

Ali MY, Uemura S, Adachi K, Itoh H, Kinosita K Jr, Ishiwata S (2002) Myosin V is a left-handed spiral motor on the right-handed actin helix. Nat Struct Biol 9(6):464–467

Ali MY, Krementsova EB, Kennedy GG, Mahaffy R, Pollard TD, Trybus KM, Warshaw DM (2007) Myosin Va maneuvers through actin intersections and diffuses along microtubules. Proc Natl Acad Sci U S A 104(11):4332–4336

Amendola V, Pilot R, Frasconi M, Maragò OM, Iatì MA (2017) Surface plasmon resonance in gold nanoparticles: a review. J Phys Condens Matter 29(20):203002

Ando T (2014) High-speed AFM imaging. Curr Opin Struct Biol 28:63–68

Ando T (2018) High-speed atomic force microscopy and its future prospects. Biophys Rev 210(2):285–292

Ando T, Uchihashi T, Kodera N (2013) High-speed AFM and applications to biomolecular systems. Annu Rev Biophys 42:393–414

Andrecka J, Ortega Arroyo J, Takagi Y, de Wit G, Fineberg A, MacKinnon L, Young G, Sellers JR, Kukura P (2015) Structural dynamics of myosin 5 during processive motion revealed by interferometric scattering microscopy. elife 4. https://doi.org/10.7554/eLife.05413.

Ashkin A, Dziedzic JM (1975) Optical levitation of liquid drops by radiation pressure. Science 187(4181):1073–1075

Ashkin A, Dziedzic JM (1985) Observation of radiation-pressure trapping of particles by alternating light beams. Phys Rev Lett 54(12):1245–1248

Ashkin A, Dziedzic JM (1987) Optical trapping and manipulation of viruses and bacteria. Science 235(4795):1517–1520

Ashkin A, Dziedzic JM (1989) Internal cell manipulation using infrared laser traps. Proc Natl Acad Sci U S A 86(20):7914–7918

Ashkin A, Dziedzic JM, Bjorkholm JE, Steven C (1986) Observation of a single-beam gradient force optical trap for dielectric particles. Opt Lett 11:288–290

Ashkin A, Dziedzic JM, Yamane T (1987) Optical trapping and manipulation of single cells using infrared laser beams. Nature 330(6150):769–771

Ashkin A, Schütze K, Dziedzic JM, Euteneuer U, Schliwa M (1990) Force generation of organelle transport measured in vivo by an infrared laser trap. Nature 348(6299):346–348

Axelrod D (2001) Selective imaging of surface fluorescence with very high aperture microscope objectives. J Biomed Opt 6(1):6–13

Axelrod D (2008) Total internal reflection fluorescence microscopy. Methods Cell Biol 89:169–221

Balci H, Ha T, Sweeney HL, Selvin PR (2005) Interhead distance measurements in myosin VI via SHRImP support a simplified hand-over-hand model. Biophys J 89(1):413–417

Baron PA, Willeke K (2001) Aerosol measurement : principles, techniques, and applications, 2nd edn. Wiley, New York/Chichester, p 463

Beausang JF, Sun Y, Quinlan ME, Forkey JN, Goldman YE (2012) Orientation and rotational motions of single molecules by polarized total internal reflection fluorescence microscopy (polTIRFM). Cold Spring Harb Protoc:pii: pdb.top069344. https://doi.org/10.1101/pdb.top069344

Beausang JF, Shroder DY, Nelson PC, Goldman YE (2013) Tilting and wobble of myosin V by high-speed single-molecule polarized fluorescence microscopy. Biophys J 104(6):1263–1273

Berg-Sørensen K, Flyvbjerg H (2004) Power spectrum analysis for optical tweezers. Rev Sci Instrum 75:594–612

Betzig E, Patterson GH, Sougrat R, Lindwasser OW, Olenych S, Bonifacino JS, Davidson MW, Lippincott-Schwartz J, Hess HF (2006) Imaging intracellular fluorescent proteins at nanometer resolution. Science 313(5793):1642–1645

Bing W, Knott A, Marston SB (2000) A simple method for measuring the relative force exerted by myosin on actin filaments in the in vitro motility assay: evidence that tropomyosin and troponin increase force in single thin filaments. Biochem J 350:693–699

Block SM, Goldstein LS, Schnapp BJ (1990) Bead movement by single kinesin molecules studied with optical tweezers. Nature 348(6299):348–352

Brizendine RK, Alcala DB, Carter MS, Haldeman BD, Facemyer KC, Baker JE, Cremo CR (2015) Velocities of unloaded muscle filaments are not limited by drag forces imposed by myosin cross-bridges. Proc Natl Acad Sci U S A 112(36):11235–11240

Brizendine RK, Sheehy GG, Alcala DB, Novenschi SI, Baker JE, Cremo CR (2017) A mixed-kinetic model describes unloaded velocities of smooth, skeletal, and cardiac muscle myosin filaments in vitro. Sci Adv 3(12):eaao2267

Capitanio M, Pavone FS (2013) Interrogating biology with force: single molecule high-resolution measurements with optical tweezers. Biophys J 105(6):1293–1303

Capitanio M, Canepari M, Cacciafesta P, Lombardi V, Cicchi R, Maffei M, Pavone FS, Bottinelli R (2006) Two independent mechanical events in the interaction cycle of skeletal muscle myosin with actin. Proc Natl Acad Sci U S A 103(1):87–92

Capitanio M, Canepari M, Maffei M, Beneventi D, Monico C, Vanzi F, Bottinelli R, Pavone FS (2012) Ultrafast force-clamp spectroscopy of single molecules reveals load dependence of myosin working stroke. Nat Methods 9(10):1013–1019

Chen L, Nakamura M, Schindler TD, Parker D, Bryant Z (2012) Engineering controllable bidirectional molecular motors based on myosin. Nat Nanotechnol 7(4):252–256

Cheney RE, O'Shea MK, Heuser JE, Coelho MV, Wolenski JS, Espreafico EM, Forscher P, Larson RE, Mooseker MS (1993) Brain myosin-V is a two-headed unconventional myosin with motor activity. Cell 75(1):13–23

Churchman LS, Okten Z, Rock RS, Dawson JF, Spudich JA (2005) Single molecule high-resolution colocalization of Cy3 and Cy5 attached to macromolecules measures intramolecular distances through time. Proc Natl Acad Sci U S A 102(5):1419–14123

Cole D, Young G, Weigel A, Sebesta A, Kukura P (2017) Label-free single-molecule imaging with numerical-aperture-shaped interferometric scattering microscopy. ACS Photonics 4(2):211–216

Coppin CM, Finer JT, Spudich JA, Vale RD (1996) Detection of sub-8-nm movements of kinesin by high-resolution optical-trap microscopy. Proc Natl Acad Sci U S A 93(5):1913–1917

Curtis ASG (1964) The mechanism of adhesion of cells to glass. J Cell Biol 20(2):199–215

Deniz AA, Mukhopadhyay S, Lemke EA (2007) Single-molecule biophysics: at the interface of biology, physics and chemistry. J R Soc Interface 5(18):15–45

Dunn AR, Spudich JA (2007) Dynamics of the unbound head during myosin V processive translocation. Nat Struct Mol Biol 14(3):246–248

Dupuis DE, Guilford WH, Wu J, Warshaw DM (1997) Actin filament mechanics in the laser trap. J Muscle Res Cell Motil 18(1):17–30

Finer JT, Simmons RM, Spudich JA (1994) Single myosin molecule mechanics: piconewton forces and nanometre steps. Nature 368(6467):113–119

Forkey JN, Quinlan ME, Goldman YE (2000) Protein structural dynamics by single-molecule fluorescence polarization. Prog Biophys Mol Biol 74(1–2):1–35

Forkey JN, Quinlan ME, Shaw MA, Corrie JE, Goldman YE (2003) Three-dimensional structural dynamics of myosin V by single-molecule fluorescence polarization. Nature 422(6930):399–404

Funatsu T, Harada Y, Tokunaga M, Saito K, Yanagida T (1995) Imaging of single fluorescent molecules and individual ATP turnovers by single myosin molecules in aqueous solution. Nature 374(6522):555–559

Furuta K, Furuta A (2018) Re-engineering of protein motors to understand mechanisms biasing random motion and generating collective dynamics. Curr Opin Biotechnol 51:39–46

Furuta A, Amino M, Yoshio M, Oiwa K, Kojima H, Furuta K (2017) Creating biomolecular motors based on dynein and actin-binding proteins. Nat Nanotechnol 12(3):233–237

Gage SH (1920) Modern dark-field microscopy and the history of its development. Trans Am Microsc Soc 39(2):95

Gardini L, Heissler SM, Arbore C, Yang Y, Sellers JR, Pavone FS, Capitanio M (2018) Dissecting myosin-5B mechanosensitivity and calcium regulation at the single molecule level. Nat Commun 9(1):2844

Gittes F, Schmidt CF (1998) Interference model for back-focal-plane displacement detection in optical tweezers. Opt Lett 23(1):7–9

Gordon MP, Ha T, Selvin PR (2004) Single-molecule high-resolution imaging with photobleaching. Proc Natl Acad Sci U S A 101(17):6462–6465

Greenberg MJ, Moore JR (2010) The molecular basis of frictional loads in the in vitro motility assay with applications to the study of the loaded mechanochemistry of molecular motors. Cytoskeleton (Hoboken) 67:273–285

Greenberg MJ, Lin T, Goldman YE, Shuman H, Ostap EM (2012) Myosin IC generates power over a range of loads via a new tension-sensing mechanism. Proc Natl Acad Sci U S A 109(37):E2433–E2440

Greenberg MJ, Lin T, Shuman H, Ostap EM (2015) Mechanochemical tuning of myosin-I by the N-terminal region. Proc Natl Acad Sci U S A 112(26):E3337–E3344

Guilford WH, Dupuis DE, Kennedy G, Wu J, Patlak JB, Warshaw DM (1997) Smooth muscle and skeletal muscle myosins produce similar unitary forces and displacements in the laser trap. Biophys J 72(3):1006–1021

Hansen PM, Tolic-Nørrelykke IM, Flyvbjerg H, Berg-Sørensen K (2006) Tweezercalib 2.1: faster version of MatLab package for precise calibration of optical tweezers. Comput Phys Commun 175:572–573

Hecht E (1998) Optics, vol 1. Addison Wesley Longman, Boston

Homsher E, Wang F, Sellers JR (1992) Factors affecting movement of F-actin filaments propelled by skeletal muscle heavy meromyosin. Am J Phys 262(3 Pt 1):C714–C723

Huang B, Wang W, Bates M, Zhuang X (2008) Three-dimensional super-resolution imaging by stochastic optical reconstruction microscopy. Science 319(5864):810–813

Hundt N, Steffen W, Pathan-Chhatbar S, Taft MH, Manstein DJ (2016) Load-dependent modulation of non-muscle myosin-2A function by tropomyosin 4.2. Sci Rep 6:20554

Hynes TR, Block SM, White BT, Spudich JA (1987) Movement of myosin fragments in vitro: domains involved in force production. Cell 48(6):953–963

Ishijima A, Doi T, Sakurada K, Yanagida T (1991) Sub-piconewton force fluctuations of actomyosin in vitro. Nature 352(6333):301–306

Ishijima A, Harada Y, Kojima H, Funatsu T, Higuchi H, Yanagida T (1994) Single-molecule analysis of the actomyosin motor using nano-manipulation. Biochem Biophys Res Commun 199(2):1057–1063

Ishijima A, Kojima H, Higuchi H, Harada Y, Funatsu T, Yanagida T (1996) Multiple- and single-molecule analysis of the actomyosin motor by nanometer-piconewton manipulation with a microneedle: unitary steps and forces. Biophys J 70(1):383–400

Ishijima A, Kojima H, Funatsu T, Tokunaga M, Higuchi H, Tanaka H, Yanagida T (1998) Simultaneous obser-

vation of individual ATPase and mechanical events by a single myosin molecule during interaction with actin. Cell 92(2):161–171

Kad NM, Trybus KM, Warshaw DM (2008) Load and pi control flux through the branched kinetic cycle of myosin V. J Biol Chem 283(25):17477–17484

Kamimura S, Takahashi K (1981) Direct measurement of the force of microtubule sliding in flagella. Nature 293(5833):566–568

Kishino A, Yanagida T (1988) Force measurements by micromanipulation of a single actin filament by glass needles. Nature 334(6177):74–76

Kitamura K, Tokunaga M, Iwane AH, Yanagida T (1999) A single myosin head moves along an actin filament with regular steps of 5.3 nanometres. Nature 397(6715):129–134

Knight AE, Veigel C, Chambers C, Molloy JE (2001) Analysis of single-molecule mechanical recordings: application to acto-myosin interactions. Prog Biophys Mol Biol 77(1):45–72

Kodera N, Ando T (2014) The path to visualization of walking myosin V by high-speed atomic force microscopy. Biophys Rev 6(3–4):237–260

Kodera N, Ando T (2018) Direct imaging of walking myosin V by high-speed atomic force microscopy. Methods Mol Biol 1805:103–122

Kodera N, Yamamoto D, Ishikawa R, Ando T (2010) Video imaging of walking myosin V by high-speed atomic force microscopy. Nature 468(7320):72–76

Kron SJ, Spudich JA (1986) Fluorescent actin filaments move on myosin fixed to glass surface. Proc Natl Acad Sci U S A 83:6272–6276

Kron SJ, Toyoshima YY, Uyeda TQ, Spudich JA (1991) Assays for actin sliding movement over myosin-coated surfaces. Methods Enzymol 196:399–416

Kukura P, Celebrano M, Renn A, Sandoghdar V (2009a) Imaging a single quantum dot when it is dark. Nano Lett 9(3):926–929

Kukura P, Ewers H, Müller C, Renn A, Helenius A, Sandoghdar V (2009b) High-speed nanoscopic tracking of the position and orientation of a single virus. Nat Methods 6(12):923–927

Laakso JM, Lewis JH, Shuman H, Ostap EM (2008) Myosin I can act as a molecular force sensor. Science 321(5885):133–136

Lauzon AM, Tyska MJ, Rovner AS, Freyzon Y, Warshaw DM, Trybus KM (1998) A 7-amino-acid insert in the heavy chain nucleotide binding loop alters the kinetics of smooth muscle myosin in the laser trap. J Muscle Res Cell Motil 19(8):825–837

Lee KG, Chen XW, Eghlidi H, Kukura P, Lettow R, Renn A, Sandoghdar V, Götzinger S (2011) A planar dielectric antenna for directional single-photon emission and near-unity collection efficiency. Nat Photonics 5:166–169

Lewalle A, Steffen W, Stevenson O, Ouyang Z, Sleep J (2008) Single-molecule measurement of the stiffness of the rigor myosin head. Biophys J 94(6):2160–2169

Liebel M, Hugall JT, van Hulst NF (2017) Ultrasensitive label-free Nanosensing and high-speed tracking of single proteins. Nano Lett 17(2):1277–1281

Limozin L, Sengupta K (2009) Quantitative reflection interference contrast microscopy (RICM) in soft matter and cell adhesion. ChemPhysChem 10(16):2752–2768

Liu C, Kawana M, Song D, Ruppel KM, Spudich JA (2018) Controlling load-dependent kinetics of β-cardiac myosin at the single-molecule level. Nat Struct Mol Biol 25(6):505–514

Mehta AD, Finer JT, Spudich JA (1997) Detection of single-molecule interactions using correlated thermal diffusion. Proc Natl Acad Sci U S A 94(15):7927–7931

Mehta AD, Rock RS, Rief M, Spudich JA, Mooseker MS, Cheney RE (1999) Myosin-V is a processive actin-based motor. Nature 400(6744):590–593

Melli L, Billington N, Sun SA, Bird JE, Nagy A, Friedman TB, Takagi Y, Sellers JR (2018) Bipolar filaments of human nonmuscle myosin 2-a and 2-B have distinct motile and mechanical properties. Elife 7:pii: e32871

Mickolajczyk KJ, Hancock WO (2018) High-resolution single-molecule kinesin assays at kHz frame rates. Methods Mol Biol 1805:123–138

Mie G (1908) Beiträge zur Optik trüber Medien, speziell kolloidaler Metallösungen. Ann Phys 330(3):377–445

Molloy JE, Burns JE, Kendrick-Jones J, Tregear RT, White DC (1995) Movement and force produced by a single myosin head. Nature 378(6553):209–212

Moore JR, Krementsova EB, Trybus KM, Warshaw DM (2001) Myosin V exhibits a high duty cycle and large unitary displacement. J Cell Biol 155(4):625–635

Nagy A, Piszczek G, Sellers JR (2009) Extensibility of the extended tail domain of processive and nonprocessive myosin V molecules. Biophys J 97(12):3123–3131

Nagy A, Takagi Y, Billington N, Sun SA, Hong DK, Homsher E, Wang A, Sellers JR (2013) Kinetic characterization of nonmuscle myosin IIb at the single molecule level. J Biol Chem 288(1):709–722

Neuman KC, Block SM (2004) Optical trapping. Rev Sci Instrum 75(9):2787–2809

Neuman KC, Nagy A (2008) Single-molecule force spectroscopy: optical tweezers, magnetic tweezers and atomic force microscopy. Nat Methods 5(6):491–505

Nishikawa S, Arimoto I, Ikezaki K, Sugawa M, Ueno H, Komori T, Iwane AH, Yanagida T (2010) Switch between large hand-over-hand and small inchworm-like steps in myosin VI. Cell 142(6):879–888

Norstrom MF, Smithback PA, Rock RS (2010) Unconventional processive mechanics of non-muscle myosin IIB. J Biol Chem 285(34):26326–26334

Ohmachi M, Komori Y, Iwane AH, Fujii F, Jin T, Yanagida T (2012) Fluorescence microscopy for simultaneous observation of 3D orientation and movement and its application to quantum rod-tagged myosin V. Proc Natl Acad Sci U S A 109(14):5294–5298

Okada T, Tanaka H, Iwane AH, Kitamura K, Ikebe M, Yanagida T (2007) The diffusive search mechanism of processive myosin class-V motor involves directional

steps along actin subunits. Biochem Biophys Res Commun 354(2):379–384

Ortega Arroyo J, Andrecka J, Spillane KM, Billington N, Takagi Y, Sellers JR, Kukura P (2014) Label-free, all-optical detection, imaging, and tracking of a single protein. Nano Lett 14(4):2065–2070

Piazzesi G, Reconditi M, Linari M, Lucii L, Bianco P, Brunello E, Decostre V, Stewart A, Gore DB, Irving TC, Irving M, Lombardi V (2007) Skeletal muscle performance determined by modulation of number of myosin motors rather than motor force or stroke size. Cell 131(4):784–795

Piliarik M, Sandoghdar V (2014) Direct optical sensing of single unlabelled proteins and super-resolution imaging of their binding sites. Nat Commun 5:4495

Ploem JS (1975) Reflection-contrast microscopy as a tool for investigation of the attachment of living cells to a glass surface. Blackwell, Oxford

Previs MJ, Beck Previs S, Gulick J, Robbins J, Warshaw DM (2012) Molecular mechanics of cardiac myosin-binding protein C in native thick filaments. Science 337(6099):1215–1218

Purcell TJ, Sweeney HL, Spudich JA (2005) A force-dependent state controls the coordination of processive myosin V. Proc Natl Acad Sci U S A 102(39):13873–13878

Qu X, Wu D, Mets L, Scherer NF (2004) Nanometer-localized multiple single-molecule fluorescence microscopy. Proc Natl Acad Sci U S A 101(31):11298–11303

Rädler J, Sackmann E (1993) Imaging optical thicknesses and separation distances of phospholipid vesicles at solid surfaces. J Phys II 3:727–748

Rädler JO, Feder TJ, Strey HH, Sackmann E (1995) Fluctuation analysis of tension-controlled undulation forces between giant vesicles and solid substrates. Phys Rev E Stat Phys Plasmas Fluids Relat Interdiscip Topics 51(5):4526–4536

Reck-Peterson SL, Yildiz A, Carter AP, Gennerich A, Zhang N, Vale RD (2006) Single-molecule analysis of dynein processivity and stepping behavior. Cell 126(2):335–348

Rief M, Rock RS, Mehta AD, Mooseker MS, Cheney RE, Spudich JA (2000) Myosin-V stepping kinetics: a molecular model for processivity. Proc Natl Acad Sci U S A 97(17):9482–9486

Ries J, Kaplan C, Platonova E, Eghlidi H, Ewers H (2012) A simple, versatile method for GFP-based super-resolution microscopy via nanobodies. Nat Methods 9(6):582–584

Rock RS, Rice SE, Wells AL, Purcell TJ, Spudich JA, Sweeney HL (2001) Myosin VI is a processive motor with a large step size. Proc Natl Acad Sci U S A 98(24):13655–13659

Rosenberg SA, Quinlan ME, Forkey JN, Goldman YE (2005) Rotational motions of macro-molecules by single-molecule fluorescence microscopy. Acc Chem Res 38(7):583–593

Ruhnow F, Zwicker D, Diez S (2011) Tracking single particles and elongated filaments with nanometer precision. Biophys J 100(11):2820–2828

Rust MJ, Bates M, Zhuang X (2006) Sub-diffraction-limit imaging by stochastic optical reconstruction microscopy (STORM). Nat Methods 3(10):793–795

Sakamoto T, Amitani I, Yokota E, Ando T (2000) Direct observation of processive movement by individual myosin V molecules. Biochem Biophys Res Commun 272(2):586–590

Sakamoto T, Wang F, Schmitz S, Xu Y, Xu Q, Molloy JE, Veigel C, Sellers JR (2003) Neck length and processivity of myosin V. J Biol Chem 278(31):29201–29207

Sakamoto T, Yildiz A, Selvin PR, Sellers JR (2005) Step-size is determined by neck length in myosin V. Biochemistry 44(49):16203–16210

Santos NC, Castanho MA (2004) An overview of the biophysical applications of atomic force microscopy. Biophys Chem 107(2):133–149

Sellers JR, Kachar B (1990) Polarity and velocity of sliding filaments: control of direction by actin and of speed by myosin. Science 249(4967):406–408

Sellers JR, Veigel C (2010) Direct observation of the myosin-Va power stroke and its reversal. Nat Struct Mol Biol 17(5):590–595

Sellers JR, Cuda G, Wang F, Homsher E (1993) Myosin-specific adaptations of the motility assay 39:23–49

Seol Y, Neuman KC (2018) Combined magnetic tweezers and micro-mirror Total internal reflection fluorescence microscope for single-molecule manipulation and visualization. Methods Mol Biol 1665:297–316

Sheetz MP, Spudich JA (1983) Movement of myosin-coated fluorescent beads on actin cables in vitro. Nature 303(5912):31–35

Sheetz MP, Block SM, Spudich JA (1986) Myosin movement in vitro: a quantitative assay using oriented actin cables from Nitella. Methods Enzymol 134:531–544

Shepherd GM, Corey DP, Block SM (1990) Actin cores of hair-cell stereocilia support myosin motility. Proc Natl Acad Sci U S A 87(21):8627–8631

Siedentopf H, Zsigmondy R (1903) Über Sichtbarmachung und Groessenbestimmung ultramikroskopischer Teilchen, mit besonderer Anwendung auf Goldrubinglaesern. Annalen der Physik 10:1–39

Smith DA, Steffen W, Simmons RM, Sleep J (2001) Hidden-Markov methods for the analysis of single-molecule actomyosin displacement data: the variance-hidden-Markov method. Biophys J 81(5):2795–2816

Snyder GE, Sakamoto T, Hammer JA 3rd, Sellers JR, Selvin PR (2004) Nanometer localization of single green fluorescent proteins: evidence that myosin V walks hand-over-hand via Telemark configuration. Biophys J 87(3):1776–1783

Sun Y, Schroeder HW 3rd., Beausang JF, Homma K, Ikebe M, Goldman YE (2007) Myosin VI walks "wiggly" on actin with large and variable tilting. Mol Cell 28(6):954–964

Sun Y, Sato O, Ruhnow F, Arsenault ME, Ikebe M, Goldman YE (2010) Single-molecule stepping and

structural dynamics of myosin X. Nat Struct Mol Biol 17(4):485–491
Sung J, Nag S, Mortensen KI, Vestergaard CL, Sutton S, Ruppel K, Flyvbjerg H, Spudich JA (2015) Harmonic force spectroscopy measures load-dependent kinetics of individual human β-cardiac myosin molecules. Nat Commun 6:7931
Sung J, Mortensen KI, Spudich JA, Flyvbjerg H (2017) How to measure load-dependent kinetics of individual motor molecules without a force-clamp. Methods Enzymol 582:1–29
Svoboda K, Schmidt CF, Schnapp BJ, Block SM (1993) Direct observation of kinesin stepping by optical trapping interferometry. Nature 365(6448):721–727
Takagi Y, Homsher EE, Goldman YE, Shuman H (2006) Force generation in single conventional actomyosin complexes under high dynamic load. Biophys J 90(4):1295–1307
Takagi Y, Farrow RE, Billington N, Nagy A, Batters C, Yang Y, Sellers JR, Molloy JE (2014) Myosin-10 produces its power-stroke in two phases and moves processively along a single actin filament under low load. Proc Natl Acad Sci U S A 111(18):E1833–E1842
Tanaka H, Ishijima A, Honda M, Saito K, Yanagida T (1998) Orientation dependence of displacements by a single one-headed myosin relative to the actin filament. Biophys J 75(4):1886–1894
Tanaka H, Homma K, White HD, Yanagida T, Ikebe M (2008) Smooth muscle myosin phosphorylated at single head shows sustained mechanical activity. J Biol Chem 283(23):15611–15618
Thompson RE, Larson DR, Webb WW (2002) Precise nanometer localization analysis for individual fluorescent probes. Biophys J 82(5):2775–2783
Toprak E, Enderlein J, Syed S, McKinney SA, Petschek RG, Ha T, Goldman YE, Selvin PR (2006) Defocused orientation and position imaging (DOPI) of myosin V. Proc Natl Acad Sci U S A 103(17):6495–6499
Uchihashi T, Scheuring S (2018) Applications of high-speed atomic force microscopy to real-time visualization of dynamic biomolecular processes. Biochim Biophys Acta Gen Subj 1862(2):229–240
Ueno H, Nishikawa S, Iino R, Tabata KV, Sakakihara S, Yanagida T, Noji H (2010) Simple dark-field microscopy with nanometer spatial precision and microsecond temporal resolution. Biophys J 98(9):2014–2023
Vale RD, Szent-Gyorgyi AG, Sheetz MP (1984) Movement of scallop myosin on Nitella actin filaments: regulation by calcium. Proc Natl Acad Sci U S A 81(21):6775–6778
Veigel C, Schmidt CF (2011) Moving into the cell: single-molecule studies of molecular motors in complex environments. Nat Rev Mol Cell Biol 12(3):163–176
Veigel C, Bartoo ML, White DC, Sparrow JC, Molloy JE (1998) The stiffness of rabbit skeletal actomyosin cross-bridges determined with an optical tweezers transducer. Biophys J 75(3):1424–1438
Veigel C, Coluccio LM, Jontes JD, Sparrow JC, Milligan RA, Molloy JE (1999) The motor protein myosin-I produces its working stroke in two steps. Nature 398(6727):530–533
Veigel C, Wang F, Bartoo ML, Sellers JR, Molloy JE (2002) The gated gait of the processive molecular motor, myosin V. Nat Cell Biol 4(1):59–65
Veigel C, Schmitz S, Wang F, Sellers JR (2005) Load-dependent kinetics of myosin-V can explain its high processivity. Nat Cell Biol 7(9):861–869
Visscher K, Gross SP, Block SM (1996) Construction of multiple-beam optical traps with nanometer-resolution position sensing. IEEE J Sel Top Quantum Electron 2(4):1066–1076
Warshaw DM, Desrosiers JM, Work SS, Trybus KM (1990) Smooth muscle myosin cross-bridge interactions modulate actin filament sliding velocity in vitro. J Cell Biol 111:453–463
Warshaw DM, Kennedy GG, Work SS, Krementsova EB, Beck S, Trybus KM (2005) Differential labeling of myosin V heads with quantum dots allows direct visualization of hand-over-hand processivity. Biophys J 88(5):L30–L32
Watanabe TM, Iwane AH, Tanaka H, Ikebe M, Yanagida T (2010) Mechanical characterization of one-headed myosin-V using optical tweezers. PLoS One 5(8):e12224
Wriedt T (2012) In: Hergert W, Wriedt T (eds) Mie theory: a review, vol 169. Springer, Berlin/Heidelberg, pp 53–71
Yanagida T, Ishii Y, Ishijima A (2011) Single-molecule measurements using microneedles. Methods Mol Biol:143–159
Yildiz A, Forkey JN, McKinney SA, Ha T, Goldman YE, Selvin PR (2003) Myosin V walks hand-over-hand: single fluorophore imaging with 1.5-nm localization. Science 300(5628):2061–2065
Yildiz A, Tomishige M, Vale RD, Selvin PR (2004a) Kinesin walks hand-over-hand. Science 303(5658):676–678
Yildiz A, Park H, Safer D, Yang Z, Chen LQ, Selvin PR, Sweeney HL (2004b) Myosin VI steps via a hand-over-hand mechanism with its lever arm undergoing fluctuations when attached to actin. J Biol Chem 279(36):37223–37226
Young G, Kukura P (2019) Interferometric scattering microscopy. Annu Rev Phys Chem 70:301–322. https://doi.org/10.1146/annurev-physchem-050317-021247
Young G, Hundt N, Cole D, Fineberg A, Andrecka J, Tyler A, Olerinyova A, Ansari A, Marklund EG, Collier MP, Chandler SA, Tkachenko O, Allen J, Crispin M, Billington N, Takagi Y, Sellers JR, Eichmann C, Selenko P, Frey L, Riek R, Galpin MR, Struwe WB, Benesch JLP, Kukura P (2018) Quantitative mass imaging of single biological macromolecules. Science 360(6387):423–427